

## Improving large-basin river routing using a differentiable Muskingum-Cunge model and physics-informed machine learning

Tadd Bindas<sup>1</sup>, Wen-Ping Tsai<sup>2</sup>, Jiangtao Liu<sup>1</sup>, Farshid Rahmani<sup>1</sup>, Dapeng Feng<sup>1</sup>, Yuchen Bian<sup>3</sup>, Kathryn Lawson<sup>1</sup>, Chaopeng Shen<sup>\*1</sup>

<sup>1</sup>Civil and Environmental Engineering, The Pennsylvania State University, PA

<sup>2</sup>Hydraulic and Ocean Engineering, National Cheng Kung University, Tainan City

<sup>3</sup> Amazon Search, Palo Alto, CA

\* Corresponding author: Chaopeng Shen, [cshen@engr.psu.edu](mailto:cshen@engr.psu.edu)

## Abstract

Recently, rainfall-runoff simulations in small headwater basins have been improved by methodological advances such as deep neural networks (NNs) and hybrid physics-NN models --- particularly, a genre called differentiable modeling that intermingles NNs with physics to learn relationships between variables. However, hydrologic routing, necessary for simulating floods in stem rivers downstream of large heterogeneous basins, had not yet benefited from these advances and it was unclear if the routing process can be improved via coupled NNs. We present a novel differentiable routing model that mimics the classical Muskingum-Cunge routing model over a river network but embeds an NN to infer parameterizations for Manning's roughness ( $n$ ) and channel geometries from raw reach-scale attributes like catchment areas and sinuosity. The NN was trained solely on downstream hydrographs. Synthetic experiments show that while the channel geometry parameter was unidentifiable,  $n$  can be identified with moderate precision. With real-world data, the trained differentiable routing model produced more accurate long-term routing results for both the training gage and untrained inner gages for larger subbasins ( $>2,000 \text{ km}^2$ ) than either a machine learning model assuming homogeneity, or simply using the sum of runoff from subbasins. The  $n$  parameterization trained on short periods gave high performance in other periods, despite significant errors in runoff inputs. The learned  $n$  pattern was consistent with literature expectations, demonstrating the framework's potential for knowledge discovery, but the absolute values can vary depending on training periods. The trained  $n$  parameterization can be coupled with traditional models to improve national-scale flood simulations.

## Main points:

1. A novel differentiable routing model can learn effective river routing parameterization, recovering channel roughness in synthetic runs.
  2. With short periods of real training data, we can improve streamflow in large rivers compared to models not considering routing.
  3. For basins  $>2,000 \text{ km}^2$ , our framework outperformed deep learning models that assume homogeneity, despite bias in the runoff forcings.

41    **1. Introduction**

42  
43    Riverine floods pose a major risk to human safety and infrastructure (Douben, 2006; François et al.,  
44    2019; International Panel on Climate Change (IPCC), 2012; Koks & Thissen, 2016) and are linked to  
45    stream channel characteristics. Riverine floods along large stem rivers occur when the peak flow rate  
46    exceeds the stem river conveyance capacity. The timing of flood convergence and peak flood rates are  
47    influenced by the channel's geometries and flow resistance properties (Candela et al., 2005; Kalyanapu  
48    et al., 2009). In recent years, we have witnessed many deadly riverine floods, e.g., in the Mississippi  
49    River, USA (Rice, 2019) and India (France-Presse, 2022), with such disasters expected to rise significantly  
50    based on future climate projections (Dottori et al., 2018; Prein et al., 2017; Winsemius et al., 2016). The  
51    ability to better account for flood convergence and streamflow processes is urgently needed to help us  
52    better inform society of stem river flood magnitudes and timing.

53

54    In hydrologic modeling, routing describes how the stream network conveys runoff downstream while  
55    accounting for mass balances and the speed of flood wave propagation (Mays, 2010). Most routing  
56    models are based on the principle of continuity (or mass conservation) but they differ in how the  
57    momentum equation or flow velocity is calculated. For example, the widely-applied Muskingum-Cunge  
58    (MC) (Cunge, 1969) routing method is a center-in-space center-in-time finite difference solution to the  
59    continuity equation, assuming a prismatic flood wave as the constitutive relationship to simplify the  
60    momentum equation. In some other cases, the momentum equation is solved in conjunction with the  
61    continuity equation (Ji et al., 2019) with a range of simplifying assumptions, e.g., ignoring inertia (Shen &  
62    Phanikumar, 2010), ignoring both inertia and pressure gradient (only slope remaining) (Mizukami et al.,  
63    2016), or including additional formulations to handle effects of scale, e.g., Li et al. (2013). In each case,  
64    these models have parameters that need to be determined from lookup tables or calibration, e.g.,  
65    roughness parameters that serve as resistance to flow.

66

67    Although routing parameters often rank among the important ones for discharge simulation (Khorashadi  
68    Zadeh et al., 2017; L. Liu et al., 2022), they been difficult to parameterize at large scales, especially in a  
69    way to both sensibly represent basin-internal spatial heterogeneity and adapt to discharge data. Using  
70    traditional roughness values tabulated for various land covers (Arcement & Schneider, 1989) requires in-  
71    situ scouting, e.g., to determine if channels have pools, weeds, grass, etc., which is currently impractical  
72    for large-scale applications. Many calibration exercises (Khorashadi Zadeh et al., 2017; L. Liu et al., 2022;

73 Mizukami et al., 2016) have used only one set of parameters for an entire basin, neglecting fine-scale  
74 spatial heterogeneity in river-reach characteristics. Some studies have employed Manning's roughness,  
75  $n$  (a coefficient representing a channel's resistance to flow), as a linear function of river depth or other  
76 characteristics (Getirana et al., 2012; H.-Y. Li et al., 2022), but it is unclear if these relationships  
77 accurately represent the available data.

78

79 While the accuracy of basin rainfall-runoff models has improved substantially in recent years with  
80 machine learning (ML) (Adnan et al., 2021; Feng et al., 2020; Kratzert et al., 2019; Sun et al., 2022; Xiang  
81 et al., 2020), these methods have not been applied to routing modules in order to benefit the simulation  
82 of stem river floods. Neural networks (NNs) like long short-term memory (LSTM), GraphWaveNet (Sun et  
83 al., 2021), or convolutional networks (Duan et al., 2020) have demonstrated their prowess in learning  
84 hydrologic dynamics from big data. They are applicable not only to streamflow hydrology but also to  
85 variables across the entire hydrologic cycle (Shen, Chen, et al., 2021; Shen & Lawson, 2021) such as soil  
86 moisture (Fang et al., 2017, 2019; J. Liu et al., 2022; O & Orth, 2021), groundwater (Wunsch et al., 2022),  
87 snow (Meyal et al., 2020), longwave radiation (Zhu et al., 2021), and water quality parameters like water  
88 temperature, dissolved oxygen and nitrogen (He et al., 2022; Hrnjica et al., 2021; Lin et al., 2022;  
89 Rahmani, Lawson, et al., 2021; Saha et al., 2023; Zhi et al., 2021). However, these approaches are mostly  
90 suitable for relatively homogeneous headwater basins; spatial heterogeneities in forcings and basin  
91 characteristics are generally not well represented in these approaches. In our previous studies we  
92 observed that large basins often turned out to have poorer performance for LSTM models. The routing  
93 module is the key component that allows us to consider how runoff from heterogeneous subbasins  
94 converge and contribute to the stem river floods, and could be extended to support reactive transport  
95 modeling in the river network.

96

97 A recent development in integrating ML with physical understanding is the use of differentiable, physics-  
98 informed machine learning models, which can approach the performance of purely data-driven ML  
99 models but also provide interpretable fluxes and states (Feng, Liu, et al., 2022). "Differentiable" models  
100 can rapidly and accurately compute the gradients of the model outputs with respect to any input,  
101 enabling the combined training of NNs to approximate complex or unknown functions from big data  
102 while keeping physical priors. Such models can be simply supported by automatic differentiation (AD),  
103 which tracks each elementary operation of tensors through the use of a computational graph, then uses  
104 derivative rules to compute the gradient of each tensor operation (Baydin et al., 2018). This enables

105 hybrid frameworks to learn and incorporate complex and potentially unknown functions from big data  
106 while retaining physical formulations. By connecting deep networks to reimplemented process-based  
107 models (or their NN surrogates), Tsai et al. (2021) developed a NN-based parameterization pipeline that  
108 infers physical parameters for process-based models. Differentiable models can also extrapolate better  
109 in space and time than purely data-driven deep networks (Feng, Beck, et al., 2022). These methods are  
110 also applicable to estimating parameters in ecosystem modeling (Aboelyazeed et al., 2022), and allow us  
111 to flexibly discover variable relationships within the model based on big data, enabling improved  
112 transparency compared to standard deep learning models.

113

114 Nevertheless, it was unclear if differentiable modeling could effectively learn relationships in a highly  
115 complex river network, which convolves and integrates processes over large scales and thus render  
116 small-scale processes unidentifiable. The river network forms a hierarchical graph, which is not unlike  
117 the graph networks for applications like social recommendations (Fan et al., 2019), but with a  
118 predefined spatial topology (due to a fixed river network) and a converging cascade. A complex river  
119 graph can have many nodes, which, when coupled with many time steps, could potentially lead to a  
120 training issue known as the vanishing gradient (Hochreiter, 1998), where the gradients with respect to  
121 the parameters are vanishingly small and the system becomes very difficult to train. Moreover, runoff  
122 data (required as an input for routing) are generally not available seamlessly for all subbasins and must  
123 be estimated by models, but models for runoff could incur substantial errors. It was unclear if the  
124 routing parameters could be learned, given such errors. It was further unclear if downstream discharge  
125 data alone has enough information to enable learning of reach-scale relationships. In other words, a  
126 reach-scale relationship may or may not be identifiable using downstream observations which integrate  
127 the signals from the entire catchment area.

128

129 In this work, we developed a novel differentiable modeling framework to perform routing and to learn a  
130 “parameterization scheme” (a systematic way of inferring parameters from more rudimentary  
131 information) for routing flows on the river network. Such a physically-based routing method has never  
132 been combined with NNs before. A NN-based parameterization scheme for Manning’s  $n$  and river  
133 bathymetry shape ( $q$ ) is integrated with MC routing and is applied throughout the river network to  
134 provide improved understanding of both the model and the modeled system. We designed synthetic  
135 and real data experiments to answer the following research questions:

- 136     1. *Given substantial errors with estimated runoff as inputs to the routing module, can we learn*  
137       *effective routing parameterization schemes that can produce reliable results for long-term*  
138       *simulations in large river networks?*
- 139     2. *Does the learned parameterization perform well for both trained and untrained internal gages*  
140       *and how does the performance vary as a function of basin area?*
- 141     3. *Do short periods of downstream discharge contain sufficient information to train a reliable*  
142       *parameterization scheme or to identify the parameterization for channel roughness and*  
143       *hydraulic geometries?*

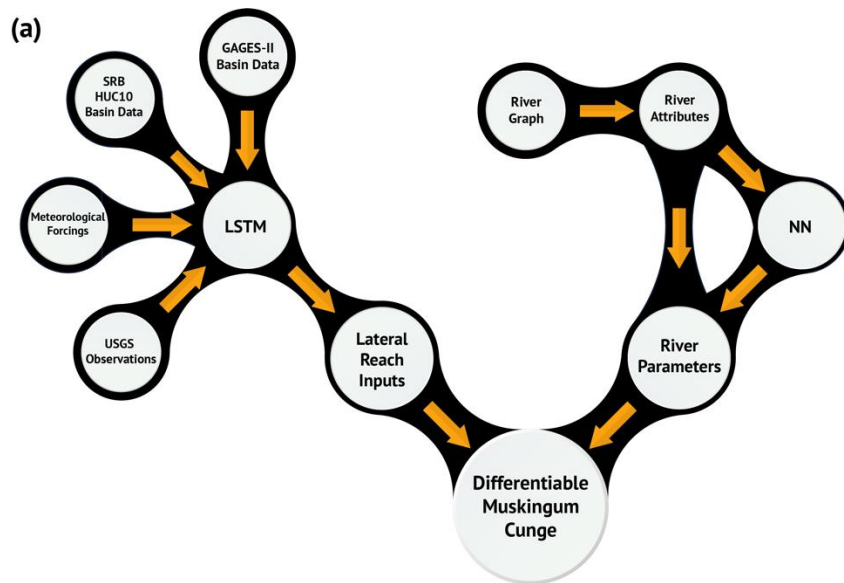
144

145 **2. Data and Methods**

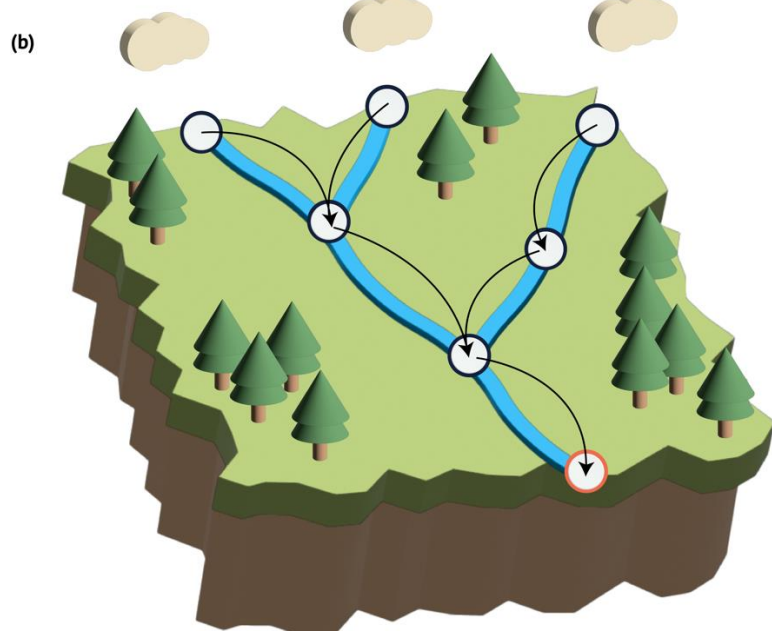
146 **2.1 Overview**

147 As an overview, we describe a differentiable model that routes runoff through a river network (or  
148 “graph” in the ML terminology) similar to the traditional Muskingum-Cunge (MC) method. But unlike the  
149 traditional MC, our differentiable model is able to incorporate and train neural networks to provide  
150 reach-scale parameterization. This new routing model can be perceived as a physics-informed graph  
151 neural network (GNN) from an ML perspective. The nodes of the graph are spaced ~2000 m apart to  
152 ensure stability. We trained an embedded a Multilayer Perceptron (MLP) NN to generate spatially-  
153 distributed river parameters for each reach (or “edge” in the GNN terminology) in the river network  
154 (Figure 1b). The loss function (the model’s goal is to minimize the output of this) was calculated at the  
155 furthest downstream node of the graph. To disentangle rainfall-runoff (required information for routing)  
156 from the routing processes, lateral inflow of combined overland and groundwater flow was obtained  
157 from a pre-trained LSTM streamflow prediction model (reported in previous work). The runoff values  
158 were then disaggregated to hourly time steps via interpolation and routed throughout the river network  
159 using the proposed differentiable routing model (Figure 1a). We provide the details in the subsections  
160 that follow.

161



162



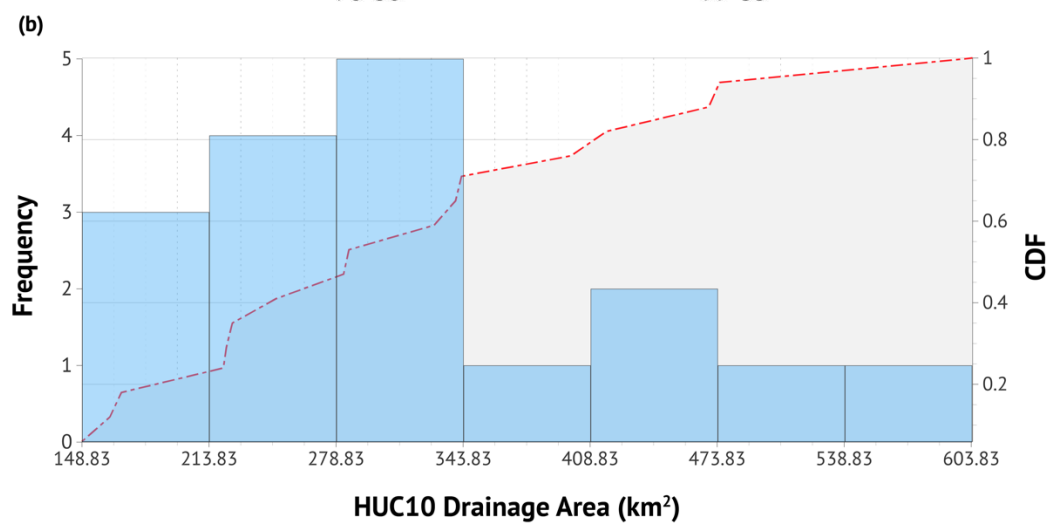
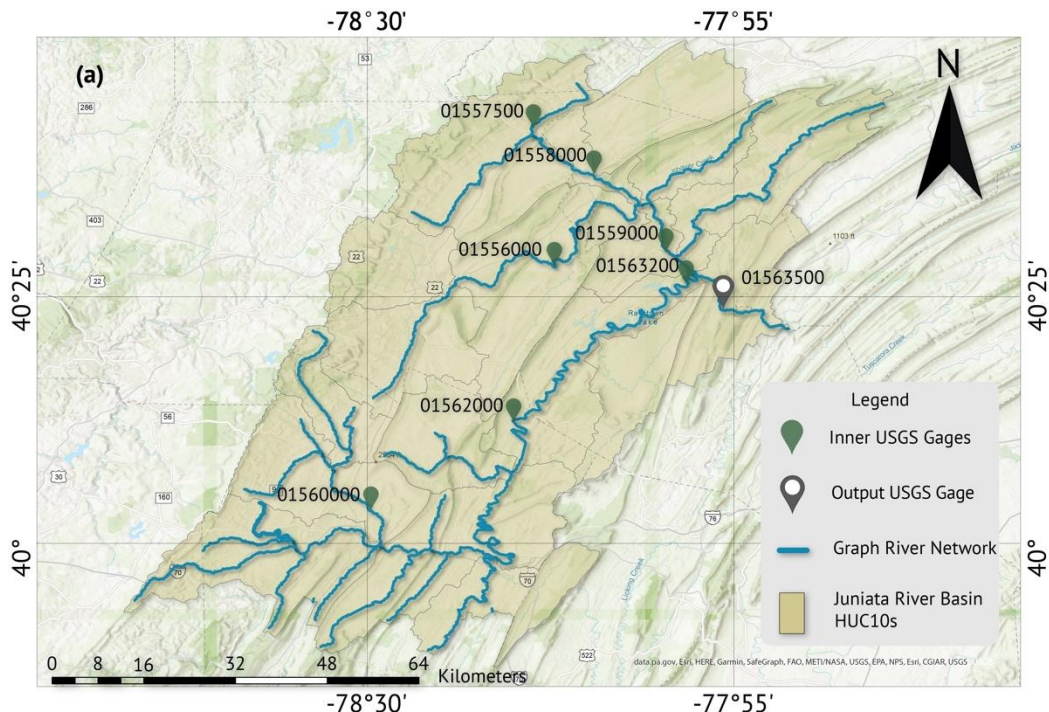
163

164

165 *Figure 1: (a) An abstract overview of how inputs move through our workflow to eventually be run*  
 166 *through the differentiable MC function. MC utilizes lateral flow inputs based on LSTM predictions, NN*  
 167 *predicted river parameters  $n$  and  $q$ , and other river attributes to generate predictions. (b) An illustration*  
 168 *of how we traverse the graph (dark blue circles) using MC to make a discharge prediction for the final*  
 169 *node (orange circle).*

170

171    2.2 *The River Graph*  
172    We constructed a river network (or graph) for the Juniata River Basin (JRB) in the northeastern United  
173    States (Figure 2), by processing the United States Geological Survey's (USGS's) National Hydrography  
174    Dataset (NHDplus v2) (HorizonSystems, 2016; Moore & Dewald, 2016) which provide topology and some  
175    attributes of the river reaches such as upstream catchment area. We ensured stability of the MC scheme  
176    by discretizing the river network into approximately 2-km reaches, resulting in 544 junction points (or  
177    nodes) and 582 river reaches (or edges). These reaches are where the physical parameters like  
178    Manning's roughness and channel shape coefficients are defined. To reduce computational demand, we  
179    selected a subset of NHDplus v2 river reaches based on a stream density threshold (total stream  
180    length/watershed area), choosing rivers with the longest length until a stream density of 0.2 km/km<sup>2</sup>  
181    was reached. We then calculated slope and sinuosity for the reaches by overlaying NHDplus v2 with 10-  
182    m resolution digital elevation data (USGS ScienceBase-Catalog, 2022). Prior work describes the bulk of  
183    the extraction procedure that prepares input data for a physically-based surface-subsurface processes  
184    model (Ji et al., 2019; Shen et al., 2013, 2014, 2016; Shen & Phanikumar, 2010).  
185  
186    The hydrograph at the furthest downstream JRB gage, USGS gage 01563500 (node 4809 in our graph) on  
187    the Juniata River at Mapleton Depot, PA, was chosen as the training target (Figure 2a). This gage has a  
188    catchment area of 5,212 km<sup>2</sup> contributed from the 582 simulated reaches upstream. Seven USGS gages  
189    are located upstream of this node which enables further validation of the simulations.  
190



195 *Figure 2: (a) A map of the Juniata River Basin's (JRB's) river network and HUC10 watersheds. Each eight-digit number corresponds to a USGS gage. (b) A histogram showing the distribution of HUC10 watersheds in the JRB. The x-axis shows the distribution of the HUC10 watershed area in square kilometers. The left y-axis shows the number of HUC10s that fall within the area ranges (corresponding with the blue bars), and the right y-axis shows a cumulative density function (CDF) distribution of the areas, corresponding with the red dashed line.*

202    2.3 Implementing River Routing with Muskingum-Cunge  
 203    2.3.1 Muskingum-Cunge  
 204    The Muskingum-Cunge (MC) method is a widely-used flood routing technique that combines the  
 205    Muskingum storage routing concept with the continuity and momentum equation for a river reach  
 206    (Cunge, 1969), solved using a center-in-space, center-in-time finite difference scheme for each reach, at  
 207    time steps  $t$  and  $t+1$ :

$$Q_{t+1} = c_1 I_{t+1} + c_2 I_t + c_3 Q_t + c_4 Q' \quad (1)$$

$$c_1 = \frac{\Delta t - 2KX}{2K(1 - X) + \Delta t} \quad (2)$$

$$c_2 = \frac{\Delta t + 2KX}{2K(1 - X) + \Delta t} \quad (3)$$

$$c_3 = \frac{2K(1 - X) - \Delta t}{2K(1 - X) + \Delta t} \quad (4)$$

$$c_4 = \frac{2\Delta t}{2K(1 - X) + \Delta t} \quad (5)$$

208    Where  $I_t$  and  $Q_t$  are the inflow and outflow of the reach at time step  $t$ , respectively, and  $I_{t+1}$  and  $Q_{t+1}$   
 209    are the inflow and outflow at the next time step,  $t+1$ .  $K$  represents travel time based on reach length  
 210    and wave celerity,  $X$  is a dimensionless inflow/outflow weighing parameter, and  $Q'$  represents lateral  
 211    inflow of the incremental catchment area of the reach, and can also include tributary inflows. We  
 212    adopted the simple linear form of the Muskingum equation:  $X$  is constant and  $K = \Delta x / v$  where  $\Delta x$  is  
 213    length of the reach and  $v$  is the discharge velocity (m/s) of the current time step. More complex  
 214    nonlinear forms of the MC equation could be tested in the future (Mays, 2019). To simulate a river  
 215    network, we divide the network into a series of reaches to route the flow of water from upstream to  
 216    downstream. The outflow from a reach is the inflow of the next downstream reach.  
 217

### 218    2.3.2 MC parameter values and variable channel dimensions

219    To implement MC, we chose an hourly time step ( $\Delta t$ ) and a weighing coefficient ( $X$ ) of 0.3, which was  
 220    based on regional expectations, for Equations 2-5. Since discharge velocity  $v$  and stream top width  $w$   
 221    vary over time, they need to be updated in each time step with respect to discharge  $Q$ , which was done  
 222    here with the help of a constitutive relationship used to close the equations. For this, because at-a-site

223 hydraulic geometries (Gleason, 2015; Leopold & Maddock, 1953) leads to a power-law relation between  
 224 top width ( $w$  [m]) and depth ( $d$  [m]), we can assume such a relationship:

$$w = pd^q \quad (6)$$

225 where  $p$  [m] and  $q$  [-] are linear and exponential parameters, respectively, that are potentially spatially  
 226 heterogeneous and represent the shape of the channel's cross-sectional area. For a rectangular channel,  
 227  $q=0$ , and for a triangular channel,  $q=1$ . The cross-sectional area  $A_{CS}$  is the integral of  $w$  with respect to  $d$   
 228 (Equation 7). To simplify the task (and because it is not sensitive based on our observations), we  
 229 assumed  $p=21$  based on preliminary data fitting to USGS hydraulic geometries from field surveys of  
 230 gages in the JRB. Note that even though we make this assumption here for model completeness, we do  
 231 not posit that  $q$  is invertible from available data because it may not be that significant for the  
 232 downstream discharge. Moving forward with these assumptions, we can write these relationships as  
 233 Equation 7:

$$A_{CS} = \int_0^d w \partial d = \int_0^d pd^q \partial d = \frac{pd^{q+1}}{q+1} \quad (7)$$

234 Combining Equation 7 with Manning's  $n$  Equation, we come up with Equation 8a. Reorganizing, we  
 235 derive a function that estimates  $d$  from  $Q$  (Equation 8b). With  $d$ ,  $p$ , and  $q$ , we can estimate  $v$  and  $K$  using  
 236 the linear form of Muskingum equation as in Equations 7, 8c, and 8d which close the equations.

$$Q = vA_{CS} = \frac{1}{n}R^{2/3}S_0^{\frac{1}{2}}\frac{pd^{q+1}}{q+1} = \frac{pd^{q+\frac{5}{3}}S_0^{\frac{1}{2}}}{n(q+1)} \quad (8a)$$

$$d = \left[ \frac{Q_t n(q+1)}{p S_0^{\frac{1}{2}}} \right]^{\frac{3}{5+3q}} \quad (8b)$$

$$v = \frac{Q_t}{A_{CS}} \quad (8c)$$

$$K = \frac{\Delta x}{v} \quad (8d)$$

237 Here,  $S_0$  represents the reach slope,  $Q_t$  represents the discharge exiting the reach at time  $t$ , and  $\Delta x$  is  
 238 the reach length.

239

240 *2.3.3 Differentiable modeling*

241 By implementing MC on a differentiable coding platform (PyTorch, Tensorflow, Julia, etc.), we can train a  
242 coupled NN in an “online” way to produce physical reach-scale river parameters for the routing model,  
243 much like our earlier work in differentiable parameter learning (dPL) (Tsai et al., 2021). Here we include  
244 a NN into the MC routing framework to optimize equation parameters based on big data while  
245 maintaining physical consistency and mass balances. In this case, a Multilayer Perceptron (MLP) (Leshno  
246 et al., 1993) is incorporated. The MLP, featuring two hidden layers and a sigmoid activation function in  
247 the output layer, accepts a normalized array of attributes ( $c$ ) for each reach (Table A2). Based on initial  
248 results, we saw no need to add further complexity (additional hidden layers). The network then outputs  
249 the Manning's roughness coefficient ( $n$ ) and channel bathymetry shape coefficient ( $q$ ):

$$n, q = NN(c) \quad (9)$$

250 where  $n$  represents a channel's resistance to flow and  $q$  represents the shape of the channel's cross-  
251 sectional area. These parameters are inferred for each reach using the attributes of that reach prior to  
252 routing, since we assumed  $n$  and  $q$  to be time-invariant. This produces  $r$  number of  $n$  and  $q$  values  
253 specific to each reach for all timesteps where  $r$  is the number of river reaches. The weights of the MLP  
254 are updated using backpropagation and the Adam optimizer (Kingma & Ba, 2017).

255

#### 256 *2.4 Lateral streamflow inputs*

257 Since spatially-distributed runoff is needed to predict runoff in downstream basins, but there is no such  
258 data, we employed a pretrained LSTM (Hochreiter & Schmidhuber, 1997) rainfall-runoff model. This  
259 LSTM model was similar to those developed and reported in previous streamflow and water quality  
260 studies (Feng et al., 2020; Ouyang et al., 2021; Rahmani, Lawson, et al., 2021; Rahmani, Shen, et al.,  
261 2021), and we refer the reader to these publications for a more detailed description of these models.  
262 After the initial training was done, we chose not to further update the LSTM in order to disentangle the  
263 rainfall-runoff and routing parts of the modeling process, testing the robustness of the methodology in  
264 the face of errors with simulated runoff. In addition, the test could tell us if other rainfall-runoff models  
265 could be used instead. Updating LSTM further could lead to its co-adaptation with the routing module,  
266 making the procedure complex.

267

268 To briefly summarize, the LSTM model used a combination of basin-averaged attributes, daily  
269 meteorological forcings, and volumetric streamflow observations as inputs, and output daily basin  
270 discharge. Meteorological forcings (total annual precipitation, downward long-wave radiation flux,

271 downward short-wave radiation flux, pressure, temperature) were obtained from the NASA NLDAS-2  
272 Forcing Data set (Xia et al., 2009, 2012). We selected 29 basin attributes (Table A1 in the Appendix)  
273 similar to those chosen in previous LSTM studies (Ouyang et al., 2021). Consistent with Ouyang et al.  
274 (2021), we focused on training the LSTM on 3213 gages selected from the USGS Geospatial Attributes of  
275 Gages for Evaluating Streamflow II (GAGES-II) dataset (Falcone, 2011) with input data between  
276 1990/01/01 - 1999/12/31. We developed the workflow to obtain forcing data and inputs seamlessly for  
277 any small basin in the conterminous United States (CONUS). In this case, we extracted data from HUC8  
278 subbasins and HUC10 watersheds to gather inputs to train our LSTM model and predict discharge,  
279 respectively.

280

281 When evaluated on the gaging stations in the study area, the model achieved a median daily Nash-  
282 Sutcliffe Efficiency (NSE) (Nash & Sutcliffe, 1970) of 0.7849 for the eight gauging stations in the JRB.  
283 After training during the period of 1990/01/01 – 1999/12/31, the model was run from 2000/01/01-  
284 2009/12/31 to predict discharge for the 17 HUC10 watersheds in the study area:

$$Q' = LSTM(x_{HUC10}, A_{HUC10}) \quad (10)$$

285 where  $Q'$  [ $\text{m}^3/\text{s}$ ] is the daily runoff for the HUC10 basin, and  $x_{HUC10}$  and  $A_{HUC10}$  are HUC10-averaged  
286 atmospheric forcings and static attribute variables, respectively. Lastly, we computed a mass transfer  
287 matrix, which tabulates the fraction of a subbasin draining into a river reach. Each row of the matrix is  
288 obtained by dividing the incremental catchment area of reaches inside a subbasin by the total area of  
289 that subbasin. Runoff can be distributed to river reaches via a simple matrix multiplication.

290

291 Due to the nature of the data used to train the LSTM, it could produce seamless (having no gaps) runoff  
292 estimates for the JRB but only on a daily, not hourly, scale. Because MC routing needs to operate on  
293 smaller time steps, we quadratically interpolated (Virtanen et al., 2020) daily data into hourly time steps,  
294 where each daily measurement occurs at 12:00 hours. For training and evaluating the routing model, we  
295 collected observed discharge data for nodes intersecting USGS GAGES-II monitoring stations. Only some  
296 time periods of the most downstream gage station were used for training, and other stations were only  
297 used for evaluation. The observed discharge data were similarly disaggregated to hourly data.

298

299    2.5 *Inverse-routing and hyperparameters*  
300    There are time zone differences between the forcing data (recorded using UTC) and USGS streamflow  
301    (recorded in UTC-5). To address this, we first shifted the LSTM-produced runoff outputs by 5 hours.  
302    Because LSTM was trained to predict runoff at the outlet of a basin, with catchment area being an  
303    impactful input to the model, it already implicitly considers the time of concentration to the outlet.  
304    However, as our modeled river network extends into the subbasins and contains smaller rivers, the  
305    routing module explicitly simulates the within-basin concentration process. Ideally, we can use an  
306    inverse-routing approach to revert LSTM-predicted runoff to the time before it enters the river network.  
307    However, as inverse-routing methods (Pan & Wood, 2013) can be quite involved and were not the focus  
308    of the study, we opted for a simple approach that shifted the runoff back in time by  $\tau$  hours.  $\tau$  is  
309    considered a hyperparameter. To avoid overfitting, we used the same  $\tau$  value for all the subbasins and  
310    all experiments, and determined this value by manually tuning based on the training period. We found  
311     $\tau = 9$  (hours) to be a good choice. More complicated procedures could be employed in the future, but  
312    this straightforward approach proved to be effective in our case.

313  
314    Hyperparameters and training period sizes for our differentiable routing model were chosen through  
315    repetitive trial and error based on the training period. These trials led us to choose a hidden size of 6 for  
316    our MLP, and a training size of eight weeks. Parameters were tuned for 50 epochs for synthetic and real  
317    data experiments. Mean Squared Error (MSE) was chosen as our loss function. Since our differentiable  
318    model at  $t=0$  assumes no inflow to the river network and relies exclusively on  $Q'$  for flow inputs, a period  
319    of 72 hours is employed to “warm up” the model states in the river network, and the loss function and  
320    NSE are not calculated within this period.

321  
322    2.6 *Experiments*  
323    2.6.1 *Synthetic Parameter Recovery*  
324    We first ran multiple synthetic parameter recovery experiments to check if the dataset and the  
325    framework could indeed recover assumed relationships with small training periods of eight weeks. Our  
326    first experiment tested if we could correctly recover a single, spatially-constant set of assumed values  
327    for both  $n$  and  $q$  for the whole river network, resulting in only two degrees of freedom. We assumed  
328    ranges from 0.01 – 0.3 and 0-3 for the synthetic values of  $n$  and  $q$ , respectively, to give a realistic value  
329    range for the MLP to learn parameters.  $n$  and  $q$  model parameters were initialized to be at the 90<sup>th</sup> and  
330    20<sup>th</sup> percentiles for the first and second set of synthetic experiments, respectfully.

331  
332 In our second experiment, we assumed constant  $n$  throughout the reaches but set the trained model as  
333  $n, q = \text{NN}(c)$  (Equation 9) so that the  $n, q$  values could be different from reach to reach. In this case,  
334 ideally, the NN would learn to output a constant value regardless of the inputs.

335  
336 Our third synthetic experiment examined if we could retrieve simple assumed relationships within  
337 realistic literature bounds (inverse-linear or power-law) [Equation 9-10] between  $n, q$ , and drainage area  
338 (DA), given that the MLP had far more inputs than just DA. The trained model is still utilizing Equation 9,  
339 as we assumed we did not know the functional relationship *a priori*.

$$n = 0.06 - 8 \times 10^{-6}(DA) \quad (11)$$
$$q = 2 - 0.00018(DA)$$

$$n = \frac{0.0915}{(DA)^{0.131}} \quad (12)$$
$$q = \frac{2.1}{(DA)^{0.357}}$$

340 *2.6.2 Observational Data Experiments.*  
341 We trained our differentiable model (updating the weights in NN as in equation 6) against observed  
342 USGS data. We utilized eight-week training periods from different years and checked whether the  
343 resulting parameters led to satisfactory routing in other years at both the training gage and untrained,  
344 inner, gages. Training periods were selected based on times when the LSTM had high accuracy and when  
345 there were frequent discharge peaks. Routing frequently fluctuating discharge through a river network  
346 introduces more variance into the MLP, allowing it to perform better when testing over a longer time  
347 period. Additionally, high LSTM accuracy reduces the noise --- we hypothesize the system has some  
348 tolerance to the runoff errors but outsized errors can invalidate the model. Periods of such “high  
349 flashiness” in the JRB occurred during both 02/01-03/29 and 11/01-12/26, while the years 2001, 2005,  
350 2007, and 2008 had high LSTM accuracy, giving us eight time periods on which to train NN models. We  
351 then trained the differentiable routing models on all eight selected time periods to determine the  
352 sensitivity of the model performance to the selected training time period.

353  
354 When interpreting model performance at inner gages, we compared results with the LSTM that modeled  
355 the whole JRB as a uniform basin and a simple summation of the  $\tau$ -shifted LSTM runoff inputs ( $Q'$ ). We  
356 also explored whether using a combination of inner gages, along with the furthest downstream gage,

357 inside of the loss function would improve model performance on all gages throughout the study area.  
358 The gages used were USGS 01560000 (edge 1053) and 01563200 (edge 2689). Internal gages were  
359 selected based on NSE metrics when using only the furthest-downstream gage in the loss calculation; we  
360 chose basins with middle-level metrics so as to not overfit the model if using highly predictive internal  
361 gages.

362

### 363 **3. Results and Discussion**

364 In the following, we first discuss our synthetic experiments (Section 3.1) which explore our routing  
365 framework's potential to retrieve assumed parameters from our differentiable GNN. Next, we show the  
366 results of confronting our model with LSTM-simulated runoff as observed streamflow at the furthest  
367 downstream gage, expanding the training period to other time ranges, then applying our models to  
368 different years for observation (Section 3.2). Furthermore, we discuss the stability of our trained models  
369 over several years of testing (Section 3.3). Lastly, we analyze the  $n$  parameters recovered for the trained  
370 models and discuss their implications (Section 3.4).

371

#### 372 *3.1 Synthetic experiments*

373 Our first synthetic experiment (with constant parameters and only 2 degrees of freedom for the search)  
374 recovered the assumed  $n$  values with moderate accuracy, but not the channel geometry parameter  $q$   
375 (Table 1). Recovered  $n$  values were within a small range of the assumed ones, with minor fluctuations,  
376 while recovered  $q$  values mostly stayed similar the initial guesses, showing slight changes after a number  
377 of iterations. This result was consistent across 10 runs, each with different "synthetic truth" values for  $n$   
378 and  $q$ . The training led  $n$  to the assumed values rapidly, typically within 20 epochs (Figure A1). The non-  
379 identifiability of  $q$  was likely because  $q$  has only a small influence on the storage capacity of the stream  
380 and the simulated discharge is not sensitive to  $q$ , making  $dL/dq$  (where  $L$  is the loss function) negligible.  
381 While it is a pity that hydraulic geometry parameters cannot be estimated, the results also implied that  
382 they would not influence the routing results noticeably. Thus, in our efforts, we focused on  $n$ .

383 *Table 1: Results from the constant synthetic  $n$  and  $q$  parameter recovery experiments*

Run	$n$			$q$		
	Initial Guess	Synthetic Truth	Recovered Parameter	Initial Guess	Synthetic Truth	Recovered Parameter
1	0.271	0.03	0.028	2.7	2	2.327

2	0.271	0.04	0.035	2.7	2	2.37
3	0.271	0.05	0.046	2.7	2.5	2.390
4	0.271	0.06	0.059	2.7	2.5	2.456
5	0.271	0.07	0.070	2.7	3	2.480
6	0.068	0.03	0.030	0.6	1.0	0.574
7	0.068	0.04	0.042	0.6	1.0	0.592
8	0.068	0.05	0.055	0.6	1.5	0.730
9	0.068	0.06	0.067	0.6	1.5	0.777
10	0.068	0.07	0.087	0.6	2.5	0.690

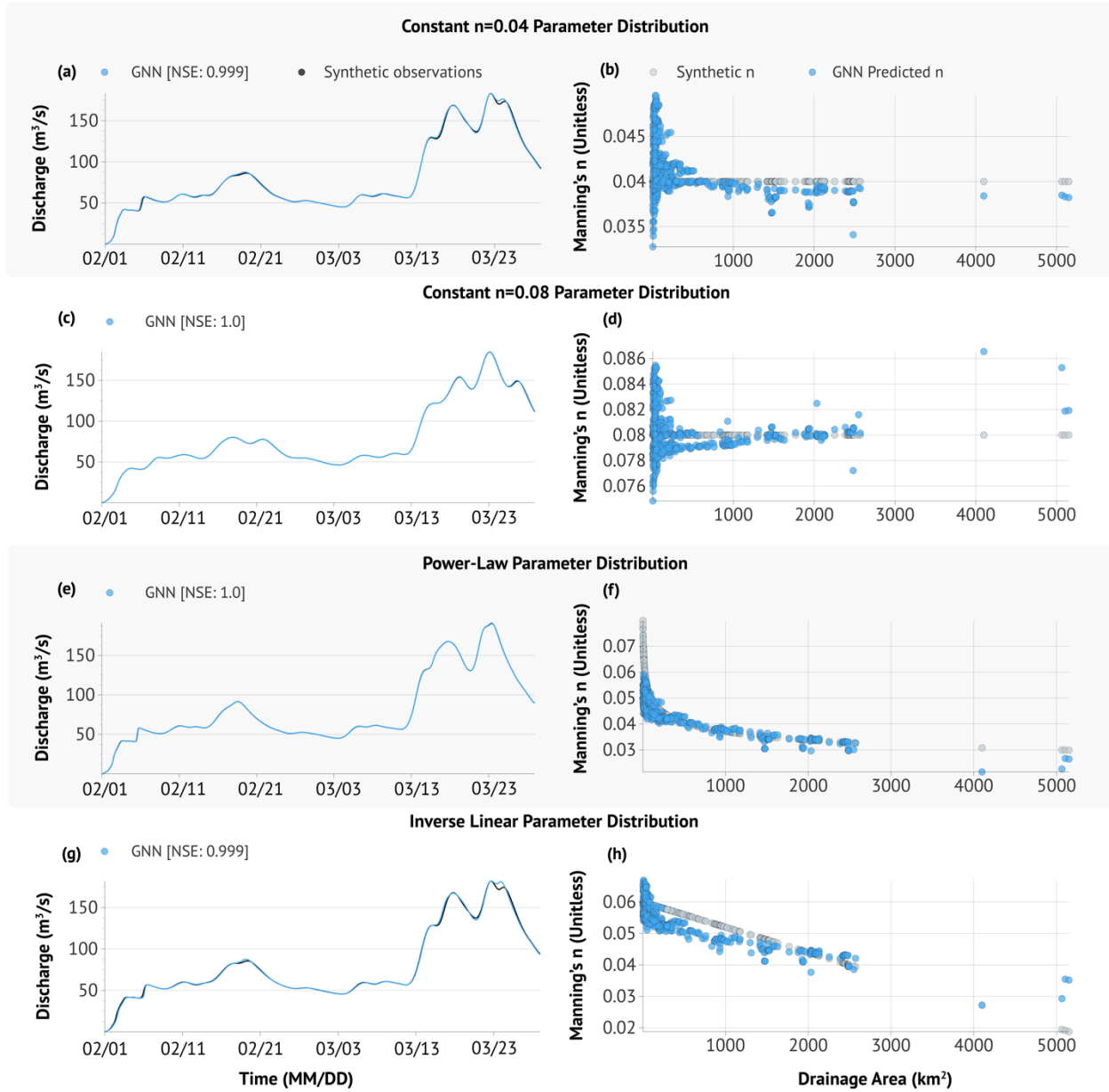
384

385 Our second synthetic experiment (assuming constant  $n$  to be recovered by NN(A)) showed that we were  
 386 able to recover the constant value that was set using an NN, but there was some scattering for the  
 387 headwater reaches (Figure 3c, 3f). We noticed trends associated with drainage area (DA), which is  
 388 correlated with reach positioning in the watershed; small DA often indicates a headwater reach, while  
 389 large DA often indicates a reach much further downstream. There were some visible differences  
 390 between the synthetic hydrographs resulting from different assumed  $n$  values (comparing Figures 3a  
 391 and 3c), which allowed the recovered  $n$  values to mostly center around the assumed value. However,  
 392 the scattering of points toward the lower-DA part of Figures 3b and 3d alluded to the fact that the  
 393 downstream discharge was strong enough to completely constraint on the model.  $n$  in different ranges  
 394 can fluctuate around the mean to generate essentially the same pattern as a constant  $n$  value.

395

396 In our third set of synthetic experiments, the simple functions could be roughly recovered for most of  
 397 the reaches, while there may have been increased uncertainty for the furthest downstream reaches  
 398 (Figure 3f & 3h). There were again noticeable differences in the hydrographs (Figures 3e & 3g) from  
 399 previous ones. When the power-law relationship was assumed, the hydrograph matched the synthetic  
 400 one almost completely (Figure 3e), and the estimated  $n$  outputs from the MLP overlapped to a great  
 401 extent with the value to be retrieved (Figure 3f). The headwater reaches (small-DA) showed a rapid  
 402 decline in  $n$  with respect to increasing DA. In the middle ranges of DA, the curve followed the assumed  
 403 one almost exactly. Toward the higher range of DA, the recovered values were lower than the assumed  
 404 relationship, but the deviation was not huge because the power-law formulation became flat in this

405 range. Based on the closeness of hydrographs in all of Figure 3, we do not anticipate that further  
406 optimization can bring significant improvement to the estimations. Similar to the two-constant-  
407 parameter retrieval experiment, the  $q$  parameter was not recoverable and thus is not shown here.  
408  
409 Based on these simple experiments, it seems training on the river graphs has some promise but also  
410 some limitations. It is promising because it is likely that  $n$  is related to DA which is, to some extent,  
411 recoverable. It is simultaneously challenging because, as a large number of reaches contribute to one  
412 gage, it is an underdetermined system. This method was not able to fully reproduce the drastic change  
413 in the low-DA range presumably because this sharp slope was inconsistent with the rest of the curve,  
414 and NNs generally do not output extreme values. It also ran into difficulty toward the high-DA range  
415 because there were simply far fewer reaches with large DA so their roles in routing were relatively  
416 minor, making the curve unconstrained in this range. This experiment informed us we should not expect  
417 values of reach-scale  $n$ , particularly in the high-DA range, to be reliable, but the overall trend may have  
418 merit, especially when we also have other constraints. These findings formed the basis for the next  
419 stage of the work where we trained  $n=NN(c)$  for real-world data. We thus expected to extract the overall  
420 patterns of  $n$  distribution but for the recovered  $q$  not to be meaningful.



421

422

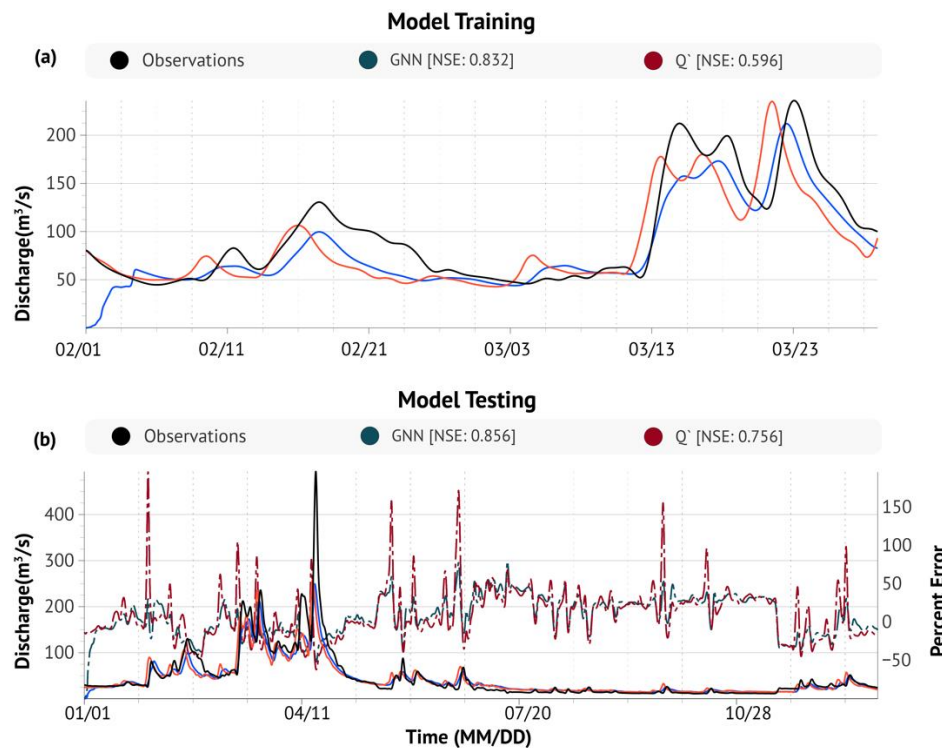
423 *Figure 3: Synthetic discharge distribution experiments. (a, c, e, g) Synthetic and modeled discharge over*  
 424 *time for various assumed relationships between  $n$  and drainage area. (b, d, f, h) Synthetic modeled*  
 425 *values of  $n$  with respect to the reach's total drainage area ( $\text{km}^2$ ). The NN can recover the overall pattern*  
 426 *but is not accurate near sharp changes or for reaches with large drainage areas. Each dot in the scatter*  
 427 *plots represents a 2-km river reach in the river network.*

428

### 429 3.2. Training on eight weeks of real data

430 The real-world data experiment showed satisfactory streamflow routing in the training period, with  
 431 improvements compared to approaches that did not employ the routing scheme, even though there

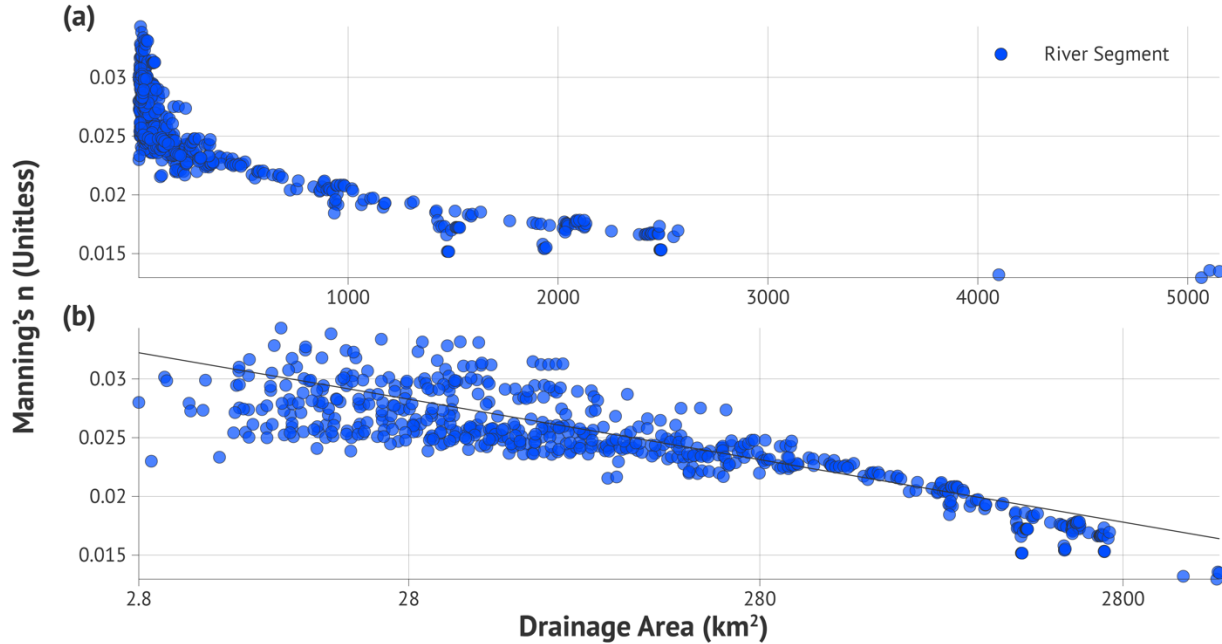
432 was significant bias in the rainfall input (Figure 4a). The hydrograph generated by the differentiable  
 433 routing model is, as expected, smoothed and delayed compared to the summation of runoffs during the  
 434 training period. Unlike the direct summation of the runoff, which has a timing difference from the  
 435 observation, the peaks of the routed hydrograph are placed almost exactly under the observed peaks,  
 436 leading to a high training NSE of 0.834. We noticed a substantial low bias in this training period,  
 437 witnessed by much lower peaks with the simulated flow compared to the observed flow. This is due to  
 438 bias in the rainfall-runoff modeling component and the mass-balance dictated by the MC formulation,  
 439 which prevents the model from adding or removing mass to remove the bias. In traditional hydrologic  
 440 model calibration, bias can be a significant concern as it can distort other parameters. In this case, we  
 441 found the model performed well even with such bias, and appropriately focused on adjusting the timing  
 442 of the flood waves. This is because the allowable adjustments were limited to routing parameters, which  
 443 blocked the model from distorting other processes.



444  
 445

446 *Figure 4: (a) Results from training the differentiable model during an eight-week period (2001) against*  
 447 *USGS observations compared with the summation of lateral inputs (denoted by Q'). (b) Results from*  
 448 *testing the trained model from Figure 4(a) over a year period (2001) compared with the summation of*  
 449 *lateral inputs. A percent error has been overlaid to the graph to show how river routing is more stable*  
 450 *than using a summation of lateral inputs.*

451  
452 The year-long test of the differentiable model yielded high metrics compared to the alternatives (Figure  
453 4b), suggesting a short calibration period could yield parameterization suitable for long-term  
454 simulations. The differentiable model obtained a year-long NSE of 0.857, which is consistent with the  
455 median NSE in the JRB. In contrast, the summation of  $Q'(\tau = 9)$  and the whole-basin *LSTM* were at  
456 0.756 and 0.801, respectively. This comparison shows that if we merely added the runoffs together  
457 (which already resolved spatial heterogeneity in runoff but not the flow process), the error due to timing  
458 could reduce NSE at the downstream gage. While the model had success with correctly timing the peak  
459 flows, it could not compensate for LSTM's errors, resulting in significant underestimation of the peak  
460 events. By design, the routing module should be detached from the errors in the runoff module.  
461  
462 Interestingly, without specific instructions, the scheme recovered a power-law-like relationship between  
463  $n$  and drainage area (DA) (Figure 5), similar to the one assumed in the synthetic case (Figure 3e &3f). The  
464  $n$  values were highest (near  $n=0.04$ ) for smaller DA and declined gradually, approaching 0.015 at the  
465 lower end. The change rate of  $n$  as a function of DA then became more gentle as DA increased. This  
466 distribution agreed well with the general understanding that headwater streams running down ridges  
467 (this region is characterized by Ridge and Valley formations) have larger slopes, higher roughness, more  
468 vegetation, and thus higher  $n$ , while the high-order streams in the valley tend to have smaller slopes and  
469 smoother beds, corresponding with lower  $n$ . In most hydrologic handbooks (Mays, 2019), a smaller  $n$  is  
470 prescribed for larger rivers.  
471



472

473 *Figure 5: The learned relationship between  $n$  and drainage area (square kilometers) for the Juniata River*  
 474 *basin according to the trained GNN. (a) The distribution on a linear scale. (b) The distribution on a*  
 475 *logarithmic scale. The network was trained for the period of 2001/02/01-2001/03/29. Each dot in the*  
 476 *scatter plot represents a 2-km river reach.*

477

### 478 3.3. Inner gage evaluation and effects of different training periods

479 Evaluating the model on the inner, untrained gages showed that the routing scheme became more  
 480 competitive compared to benchmark levels as for downstream gages (Table 2). As for the benchmarks,  
 481 the uniform LSTM (the catchment area of each gage is consider a basin and basin-averaged  
 482 forcing/attributes were used as inputs to the trained LSTM to simulate flow at the gage) already  
 483 attempts to consider routing internally but does not consider rainfall/attribute spatial heterogeneity,  
 484 while the summation of  $Q'$  (runoffs were simulated from multiple HUC10 basins and added together)  
 485 considers the spatial heterogeneity but not routing in the stem river. For 2 of the 4 gages with larger  
 486 than  $\sim 2000 \text{ km}^2$  of catchment area, the differentiable routing model performed noticeably better than  
 487 the uniform LSTM models for them (for the other two, they were about the same). For the three  
 488 midsized subbasins ( $500-2000 \text{ km}^2$ ), the comparisons were mixed. For the small subbasins, and  
 489 especially gage 01557500 ( $94.8 \text{ km}^2$ ), the uniform LSTM was noticeably better. The subbasin for  
 490 01557500 is smaller than our runoff-producing unit (HUC10s, with the smallest one  $\sim 200 \text{ km}^2$ ). This  
 491 means predictions below this threshold can be error-prone. Our model was also better than the

492 summation of Q' for 7 of the 8 gages and the gap was larger for downstream gages (Table 2), suggesting  
493 the flow convergence process matters more and more as we go downstream.

494

495 When we used multiple internal gages within the NN loss function, results improved very slightly at  
496 smaller DA gages, while degraded barely noticeably at larger DA reaches. Overall, the differences are too  
497 small to have real-world implications, but we can still observe the pattern that the multi-gage calibration  
498 appears to produce a slightly more balanced model that improves simulations at some previously  
499 weakly-simulated tributaries, at a (very minor) cost at the most downstream one. This small tradeoff  
500 may be due to spatial errors in forcing data. As the model explicitly simulates flows in all modeled  
501 reaches, the differentiable model provides a way to absorb data from as many stations as possible, if the  
502 ungauged regions are important to the users.

503

504 *Table 2: Internal gage NSE values for the year 2001, with the rows ranked by the size of the subbasin  
505 from small to large. The differentiable routing model was trained on the period from 2001/02/01-  
506 2001/03/29 calculating loss from the final gage but the LSTM was trained using >3000 CONUS gages.  
507 We include the LSTM NSE to show how the use of routing compares to just using LSTM predictions. Bold  
508 font indicates the top performing model for each gage.*

Edge ID	Gage Number	Basin Drainage Area (km <sup>2</sup> )	Uniform LSTM	Q` Runoff NSE ( $\tau = 9$ )	Differentiable routing model ( $\tau = 9$ )	Multiple Gage Loss for differentiable routing ( $\tau = 9$ )
1280	01557500	94.8	<b>0.8149</b>	0.5575	0.5623	0.5627
1053	01560000	440.5	<b>0.7028</b>	0.6054	0.6578	0.6625
2799	01558000	542.1	<b>0.8201</b>	0.7473	0.6963	0.6981
4780	01556000	723.5	0.6624	0.6568	0.6937	<b>0.6957</b>
2662	01562000	1943.5	0.7957	0.6857	0.7942	<b>0.7977</b>
4801	01559000	2103.0	0.7815	0.7449	0.8136	<b>0.8172</b>

2689	01563200	2482.9	0.5703	0.6497	<b>0.7831</b>	0.7773
4809	01563500	5212.8	0.8024	0.7563	<b>0.857</b>	0.8546

509

510 The above comparisons informed us of the favorable and unfavorable ranges of applicability for our  
 511 workflow: the differentiable model found competitive advantages for stem rivers with catchments  
 512 greater than 2,000 km<sup>2</sup>, but may run into issues for scales smaller than the smallest runoff-producing  
 513 unit (HUC10, around 200 km<sup>2</sup>). The issues for the smallest basins could be attributed to the procedure  
 514 that transfers mass from subbasin to regular grids on the river network, which should be improved in  
 515 future work. As a result, the smallest headwater basins are best to be directly simulated by the uniform  
 516 LSTM models. Also, smaller runoff-generating units could be used in the future to mitigate this issue.  
 517 The advantages of the differentiable routing model over the uniform LSTM for larger basins were due to  
 518 resolving the heterogeneity in rainfall and basin static attributes as well as better representing routing.  
 519 The uniform LSTM can internally represent some flow lags but it appears less effective as basin size  
 520 increases.

521

522 The results imply that the advantages will increase for even larger basins, where currently LSTM does  
 523 not apply well, along with basins where rainfall heterogeneity makes a big difference. The JRB is situated  
 524 in the northeastern part of the CONUS; many other regions may exhibit more prominent effects of  
 525 heterogeneity. For example, past studies have always found it difficult to simulate large basins on the  
 526 northern and central Great Plains (Feng et al., 2020; Martinez & Gupta, 2010), potentially due to  
 527 spatially-concentrated rainfall and runoff generation (Fang & Shen, 2017). Also, in the mountainous  
 528 areas of the CONUS Northwest and Southeast, orographic precipitation could have significant spatial  
 529 concentration. We hypothesize applying models to smaller basins and incorporating the routing scheme  
 530 will allow these regions to be better modeled.

531

532 As expected, the training periods selected can exert an influence on the model, but as long as we used  
 533 reasonable training periods, the results were acceptable. When the scheme was trained on eight-week  
 534 periods from different years, it generated somewhat different but mostly functional parameterizations  
 535 (Figure A2 in the Appendix), unless it was trained in some unreasonable training periods where the  
 536 LSTM had drastic differences from the observed outflows (Table 3). The maximum achievable NSEs for  
 537 the years of 2001, 2005, 2007, and 2008 were 0.857, 0.87, 0.827, and 0.787, respectively, with all

538 models outperforming Q` NSE values for their respective periods (Table A3 in the Appendix). We found  
 539 that if the models were trained on other periods (2001a, 2001b, 2005b, 2007a), the test NSEs were  
 540 mostly decent, and at least not drastically worse. However, choosing 2007b or 2008a led to notably  
 541 inferior results (Figure 6b-e). Examining the characteristics of the different training periods, we see that  
 542 the problematic training periods did not contain full flood rise and recession phases (Figure 6a & 6b). As  
 543 a result, 2007b and 2008a as training periods led to either the lowest or the highest  $n$  values and also  
 544 had relatively low NSE values (Figure A2 in the Appendix). Similarly, training period 2005a gave relatively  
 545 large  $n$  values which also resulted in suboptimal (although still decent) results in all the years. Hence, we  
 546 need to pick periods that (i) contain full flood rise and recession phases; and (ii) have high runoff NSEs.  
 547 In addition, even though the routing simulation can be improved by short training periods, the spread of  
 548 estimated  $n$  again shows that the identification of  $n$  via small training periods can be difficult. Future  
 549 work could employ longer training periods to compromise across different periods and obtain broadly-  
 550 performant parameterization. However, another possibility is that  $n$  itself can vary over time, which  
 551 would be an orthodoxy but not unthinkable idea.

552

553

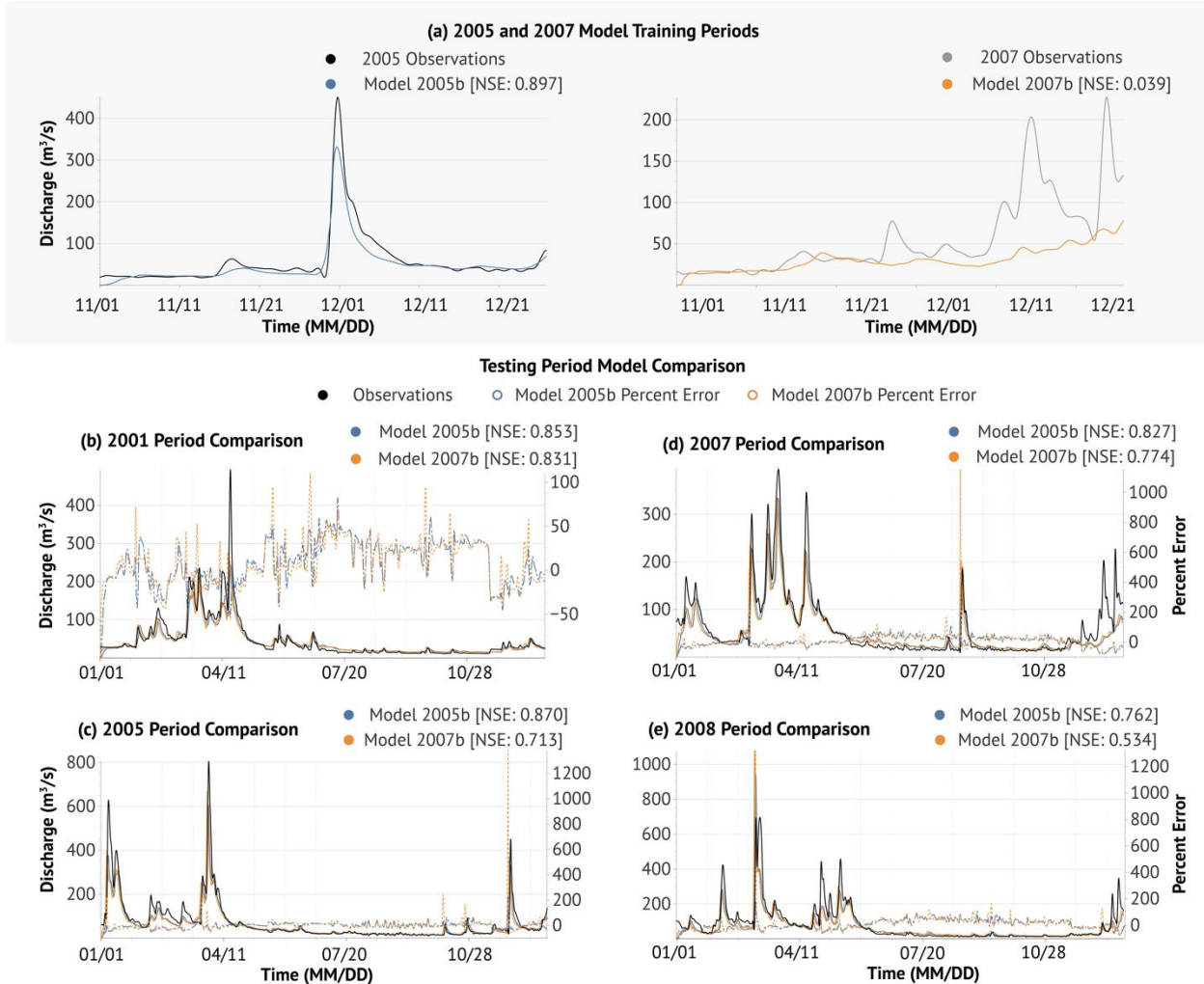
554

555 *Table 3. The NSE values correspond to testing differentiable models on different test years. Bold font*  
 556 *indicates the highest NSE, while underlined metrics indicate the lowest (noticeably worse than obtained*  
 557 *from other periods) for the testing period.*

558

Testing Period	Training Period							
	2001a 02/01-3/29	2001b 11/01-12/26	2005a 02/01-3/29	2005b 11/01-12/26	2007a 02/01-3/29	2007b 11/01-12/26	2008a 02/01-3/29	2008b 11/01-12/26
2001	<b>0.857</b>	0.845	0.850	0.853	0.857	0.831	<u>0.782</u>	0.856
2005	0.797	0.828	0.843	<b>0.870</b>	0.816	<u>0.713</u>	0.785	0.785
2007	0.815	0.812	0.821	<b>0.827</b>	0.819	0.774	<u>0.753</u>	0.813
2008	0.643	0.715	0.723	0.762	0.676	<u>0.534</u>	<b>0.787</b>	0.623
Average	0.778	0.800	0.809	<b>0.828</b>	0.792	<u>0.713</u>	0.777	0.769

559  
560



561  
562  
563  
564  
565  
566  
567

Figure 6: (a) Two training periods: 2005 and 2007a. The former contains a full rising-recession cycle while the latter does not have a complete cycle for training, thus leading to larger errors during test. The solid line indicates the training of Model 2005b while the dashed line indicates Model 2007b during the time period of 11/01-12/27 during the years 2005 and 2007, respectively. (b-c) Test periods for these two models: (b) 2001, (c) 2005, (d) 2007, and (e) 2008. For (b-e) the solid line indicates discharge while the dashed line indicates percent error of each model's output compared with the observations.

568  
569  
570  
571  
572

### 3.4. Further discussion

Although the estimated  $n$  values were both functional for routing streamflow and physically meaningful, the results suggest the downstream discharge only poses a moderate constraint on the  $n$  values, and short training periods may not be sufficient to identify the true  $n$  values. Hence, while our procedure can

573 obtain  $n$  parameterization performant for long-term simulations, we do not claim that the procedure  
574 retrieved the “true”  $n$  parameterization. Especially considering there are many input variables to the NN  
575 that covary in space, it may be difficult to disentangle causation from correlation. Due to the lack of  
576 ground truth for  $n$  in the real-data case, we leave this evaluation for future effort as we compile more  
577 measurement data. Recall that we were able to retrieve the overall pattern of  $n$  in the synthetic  
578 experiments but faced large uncertainties in some areas of the parameter space. This is attributed to the  
579 numerous degrees of freedom (a high-dimensional input space for the NN, influencing many reaches)  
580 constrained by only one downstream output with a relatively short training period. Nevertheless, this  
581 training is valuable because discharge data can be widely available, and we will be able to employ it in  
582 conjunction with other constraints, e.g., scattered measurements or expert-specified relationships.

583

584 Regarding other potential recoverable parameters, we suspect the dimensionless MC inflow/outflow  
585 weighing parameter  $X$ , which indicates the shape of the assumed flood prism, cannot be identified for  
586 the same reason as  $q$  --- the geometries of the channel do not impact flow rates in a meaningful way.  
587 Future work could investigate if learning it produces any benefit. Similarly, linear channel coefficient  $p$   
588 values were also never recoverable in single parameter tests and decreased resulting NSE values when  
589 used as a tunable parameter. Thus, we did not include it in this study. In addition, we hypothesize using  
590 more complex MC formula, e.g., the nonlinear form of the Cunge equation (the celerity is defined as  
591  $dQ/dA$ ), which might add to numerical challenges for large-scale simulations, would lead to different  $n$   
592 values, as the recovered values are inherently linked to the inverse model employed.

593

594 Here we employed a static parameterization scheme for  $n$ , following the conventional approach.  
595 However, the framework allows for the use of a dynamic  $n$  (likely dependent on  $Q$ ). It is not clear if we  
596 must use a static parameterization as done conventionally, as some previous studies have found a  
597 dynamic  $n$  to offer better results (Ye et al., 2018). In the future, it will be interesting to see if a dynamical  
598  $n$  parameterization could significantly impact the routing results. On another note, we chose an eight-  
599 week time period as our training length as a probe to assess the required training duration and selection  
600 criteria for such periods. We trained eight different models (Section 3.3) on different time periods and  
601 showed that the choice of training period timing, and LSTM performance for the inputs played  
602 important roles. Future effort should include longer training periods to most robustly estimate the  
603 parameters.

604

605 When investigating the impact of multiple gages, rather than a single downstream-most gage (in model  
606 loss calculation and parameter updates), results were very similar in terms of NSE score and recovered  
607 Manning's  $n$  parameters. We believe this may be because the JRB is a relatively small river network, so  
608 internal gage observations are highly correlated in discharge volume ( $\text{m}^3/\text{s}$ ) and fluctuation (storm event  
609 timing). Adding more gages could be useful if flows in different parts of the basin need to be accurately  
610 reported, but may be less important if only the downstream gage is of concern.

611  
612 Our approach, akin to a classical routing scheme, is modular --- the trained weights of the NN that  
613 generates  $n$  are not tied to a particular runoff model. Our work can be coupled to traditional models in  
614 multiple ways. Firstly, the trained network can be used to generate  $n$  for traditional models. In this way,  
615 no change is required on the part of the traditional models. Secondly, the neural network and the  
616 trained weights can be ported to other programming environments like Fortran. This makes it possible  
617 to use the trained parameterizations as a built-in module in continental-scale models (Greuell et al.,  
618 2015; Johnson et al., 2019; Regan et al., 2018). An alternative approach is to lump both the routing and  
619 runoff simulations into one problem and optimize them together, as demonstrated in some other  
620 studies (Jia et al., 2021). In our case, this would mean that we would train both the runoff LSTM and the  
621 routing module together. In many big-data DL case studies, lumped models tend to have higher  
622 performance compared to a workflow that separates the tasks into multiple minor tasks. However, in  
623 our case here, this leads to coadaptation concerns. Moreover, our approach is modular so it can be  
624 easily coupled to other runoff models, e.g., a non-differentiable traditional model, or a differentiable  
625 one (Feng, Beck, et al., 2022; Feng, Liu, et al., 2022).

626  
627 **4. Conclusions**  
628 In this work, we used a combination of a pre-trained LSTM rainfall-runoff model and Muskingum-Cunge  
629 routing to create a learnable routing model, or, from the perspective of machine learning, a physics-  
630 informed graph neural network. This model predicts streamflow in stem rivers and learn river  
631 parameters throughout a river network, which is urgently needed to improve the next-generation large-  
632 scale hydrologic models. Because our framework is built on physical principles and estimates widely-  
633 used  $n$  values, it can be easily ported to work with other models. For example, the trained NN and the  
634 weights can be loaded into Fortran or C programs to support traditional hydrologic models or routing  
635 schemes, e.g. (H. Li et al., 2013; Mizukami et al., 2016). Our synthetic experiments recovered the overall  
636 spatial pattern of  $n$  with moderate accuracy but could not recover the channel cross-sectional geometry

637 parameter ( $q$ ). Furthermore, our synthetic experiments yielded promising results in recovering synthetic  
638  $n$  and drainage area relationships, implying there is potential to learn reach-scale physics in the river  
639 network using differentiable modeling.

640

641 With the real-world data, short-term training periods of downstream hydrographs can produce  $n$   
642 parameterization that improve long-term routing results, but may be insufficient to constrain the  $n$   
643 values more precisely than a general spatial pattern. Eight weeks of real-world data produced decent  
644 long-term streamflow routing and improved upon approaches that did not use routing, yet training on  
645 different periods could result in somewhat different distributions. When looking at the  $n$  vs drainage  
646 area distribution attained by our trained model against USGS observations, we found that the  $n$  values  
647 agreed with the literature bounds for the area, but the absolute magnitudes may fluctuate depending  
648 on the training period. Besides using longer training periods to obtain  $n$  values that compromise across  
649 periods, future work should also consider if  $n$  should be treated as dynamic in time. Further work can  
650 expand this analysis to other basins with different conditions (streams outside of the Ridge and Valley  
651 physiographic division of the CONUS) to see if the model can still identify their trends correctly.  
652 Reviewing the internal gage NSE scores over a full year of data showed a correlation between drainage  
653 area and the relative advantage of our routing scheme, highlighting the impacts of heterogeneity and  
654 flow convergence.

655

656

## 657 **Open Research**

658 The LSTM streamflow model code (Feng et al., 2020; Ouyang et al., 2021) relevant to this work can be  
659 accessed via Zenodo (Shen, Fang, et al., 2021). The differentiable routing model will be made available  
660 to reviewers upon a paper revision request, and a new Zenodo release will be published upon paper  
661 acceptance. All datasets used are publicly available, including the GAGES-II dataset (Falcone, 2011),  
662 NHDPlus (HorizonSystems, 2016), and NLDAS (Xia et al., 2012). Other data sources can be found in Table  
663 A1.

664

## 665 **Funding Acknowledgements**

666 Funding was awarded to Cooperative Institute for Research to Operations in Hydrology (CIROH) through  
667 the NOAA Cooperative Agreement with The University of Alabama (NA22NWS4320003).

668

- 669
- 670 **References**
- 671 Aboelyazeed, D., Xu, C., Hoffman, F. M., Jones, A. W., Rackauckas, C., Lawson, K. E., & Shen,  
672 C. (2022). A differentiable ecosystem modeling framework for large-scale inverse  
673 problems: demonstration with photosynthesis simulations. *Biogeosciences Discussions*.  
674 <https://doi.org/10.5194/bg-2022-211>
- 675 Adnan, R. M., Petroselli, A., Heddam, S., Santos, C. A. G., & Kisi, O. (2021). Comparison of  
676 different methodologies for rainfall–runoff modeling: machine learning vs conceptual  
677 approach. *Natural Hazards*, 105(3), 2987–3011. <https://doi.org/10.1007/s11069-020-04438-2>
- 679 Arcement, G. J., & Schneider, V. R. (1989). *Guide for Selecting Manning's Roughness  
680 Coefficients for Natural Channels and Flood Plains* (Water-Supply Paper No. 2339). U.S.  
681 Geological Survey. Retrieved from <https://pubs.usgs.gov/wsp/2339/report.pdf>
- 682 Baydin, A. G., Pearlmutter, B. A., Radul, A. A., & Siskind, J. M. (2018). Automatic differentiation  
683 in machine learning: A survey. *Journal of Machine Learning Research*, 18(153), 1–43.  
684 Retrieved from <http://jmlr.org/papers/v18/17-468.html>
- 685 Candela, A., Noto, L. V., & Aronica, G. (2005). Influence of surface roughness in hydrological  
686 response of semiarid catchments. *Journal of Hydrology*, 313(3), 119–131.  
687 <https://doi.org/10.1016/j.jhydrol.2005.01.023>
- 688 Carabajal, C. C., & Harding, D. J. (2006). SRTM C-Band and ICESat laser altimetry elevation  
689 comparisons as a function of tree cover and relief. *Photogrammetric Engineering &  
690 Remote Sensing*, 72(3), 287–298. <https://doi.org/10/ggj69r>
- 691 Chaney, N. W., Minasny, B., Herman, J. D., Nauman, T. W., Brungard, C. W., Morgan, C. L. S.,  
692 et al. (2019). POLARIS Soil Properties: 30-m Probabilistic Maps of Soil Properties Over  
693 the Contiguous United States. *Water Resources Research*, 55(4), 2916–2938.  
694 <https://doi.org/10/ggj68b>

- 695 Cunge, J. A. (1969). On the subject of a flood propagation computation method (Muskingum  
696 method). *Journal of Hydraulic Research*, 7(2), 205–230.  
697 <https://doi.org/10.1080/00221686909500264>
- 698 Dottori, F., Szewczyk, W., Ciscar, J.-C., Zhao, F., Alfieri, L., Hirabayashi, Y., et al. (2018).  
699 Increased human and economic losses from river flooding with anthropogenic warming.  
700 *Nature Climate Change*, 8(9), 781–786. <https://doi.org/10.1038/s41558-018-0257-z>
- 701 Douben, K.-J. (2006). Characteristics of river floods and flooding: a global overview, 1985–  
702 2003. *Irrigation and Drainage*, 55(S1), S9–S21. <https://doi.org/10.1002/ird.239>
- 703 Duan, S., Ullrich, P., & Shu, L. (2020). Using convolutional neural networks for streamflow  
704 projection in California. *Frontiers in Water*, 2. <https://doi.org/10.3389/frwa.2020.00028>
- 705 Falcone, J. A. (2011). GAGES-II: Geospatial Attributes of Gages for Evaluating Streamflow  
706 [Data set]. *GAGES-II: Geospatial Attributes of Gages for Evaluating Streamflow*. USGS  
707 Unnumbered Series, Reston, VA: U.S. Geological Survey.  
708 <https://doi.org/10.3133/70046617>
- 709 Fan, W., Ma, Y., Li, Q., He, Y., Zhao, E., Tang, J., & Yin, D. (2019, November 22). Graph neural  
710 networks for social recommendation. arXiv. <https://doi.org/10.48550/arXiv.1902.07243>
- 711 Fang, K., & Shen, C. (2017). Full-flow-regime storage-streamflow correlation patterns provide  
712 insights into hydrologic functioning over the continental US. *Water Resources Research*,  
713 53(9), 8064–8083. <https://doi.org/10.1002/2016WR020283>
- 714 Fang, K., Shen, C., Kifer, D., & Yang, X. (2017). Prolongation of SMAP to spatiotemporally  
715 seamless coverage of continental U.S. using a deep learning neural network.  
716 *Geophysical Research Letters*, 44(21), 11,030-11,039.  
717 <https://doi.org/10.1002/2017gl075619>
- 718 Fang, K., Pan, M., & Shen, C. (2019). The value of SMAP for long-term soil moisture estimation  
719 with the help of deep learning. *IEEE Transactions on Geoscience and Remote Sensing*,  
720 57(4), 2221–2233. <https://doi.org/10.1109/TGRS.2018.2870333>

- 721 Feng, D., Fang, K., & Shen, C. (2020). Enhancing streamflow forecast and extracting insights  
722 using long-short term memory networks with data integration at continental scales.  
723 *Water Resources Research*, 56(9), e2019WR026793.  
724 <https://doi.org/10.1029/2019WR026793>
- 725 Feng, D., Liu, J., Lawson, K., & Shen, C. (2022). Differentiable, learnable, regionalized process-  
726 based models with multiphysical outputs can approach state-of-the-art hydrologic  
727 prediction accuracy. *Water Resources Research*, 58(10), e2022WR032404.  
728 <https://doi.org/10.1029/2022WR032404>
- 729 Feng, D., Beck, H., Lawson, K., & Shen, C. (2022). The suitability of differentiable, learnable  
730 hydrologic models for ungauged regions and climate change impact assessment.  
731 *Hydrology and Earth System Sciences Discussions*, 1–28. <https://doi.org/10.5194/hess-2022-245>
- 733 France-Presse, A. (2022, June 19). At least 59 dead and millions stranded as floods devastate  
734 India and Bangladesh. *The Guardian*. Retrieved from  
735 <https://www.theguardian.com/world/2022/jun/18/at-least-18-dead-and-millions-stranded-as-floods-devastate-india-and-bangladesh>
- 737 François, B., Schlef, K. E., Wi, S., & Brown, C. M. (2019). Design considerations for riverine  
738 floods in a changing climate – A review. *Journal of Hydrology*, 574, 557–573.  
739 <https://doi.org/10.1016/j.jhydrol.2019.04.068>
- 740 Friedl, M., & Sulla-Menashe, D. (2019). MCD12Q1 MODIS/Terra+Aqua Land Cover Type Yearly  
741 L3 Global 500m SIN Grid V006 [Data set].  
742 <https://doi.org/10.5067/MODIS/MCD12Q1.006>
- 743 Getirana, A. C. V., Boone, A., Yamazaki, D., Decharme, B., Papa, F., & Mognard, N. (2012).  
744 The Hydrological Modeling and Analysis Platform (HyMAP): Evaluation in the Amazon  
745 Basin. *Journal of Hydrometeorology*, 13(6), 1641–1665. <https://doi.org/10.1175/jhm-d-11-0102.1>

- 746 Gleason, C. J. (2015). Hydraulic geometry of natural rivers: A review and future directions.
- 747 *Progress in Physical Geography*. <https://doi.org/10/f7dsqm>
- 748 Greuell, W., Andersson, J. C. M., Donnelly, C., Feyen, L., Gerten, D., Ludwig, F., et al. (2015).
- 749 Evaluation of five hydrological models across Europe and their suitability for making
- 750 projections under climate change. *Hydrology and Earth System Sciences Discussions*,
- 751 12(10), 10289–10330. <https://doi.org/10.5194/hessd-12-10289-2015>
- 752 He, M., Wu, S., Huang, B., Kang, C., & Gui, F. (2022). Prediction of total nitrogen and
- 753 phosphorus in surface water by deep learning methods based on multi-scale feature
- 754 extraction. *Water*, 14(10), 1643. <https://doi.org/10.3390/w14101643>
- 755 Hochreiter, S. (1998). The vanishing gradient problem during learning recurrent neural nets and
- 756 problem solutions. *International Journal of Uncertainty, Fuzziness and Knowledge-Based Systems*, 06(02), 107–116. <https://doi.org/10.1142/S0218488598000094>
- 757 Hochreiter, S., & Schmidhuber, J. (1997). Long Short-Term Memory. *Neural Computation*, 9(8),
- 759 1735–1780. <https://doi.org/10.1162/neco.1997.9.8.1735>
- 760 HorizonSystems. (2016). NHDPlus version 2 [Data set]. Retrieved from [http://www.horizon-](http://www.horizon-systems.com/nhdplus/NHDplusV2_home.php)
- 761 [systems.com/nhdplus/NHDplusV2\\_home.php](http://www.horizon-systems.com/nhdplus/NHDplusV2_home.php)
- 762 Hrnjica, B., Mehr, A. D., Jakupović, E., Crnkić, A., & Hasanagić, R. (2021). Application of deep
- 763 learning neural networks for nitrate prediction in the Klokoč River, Bosnia and
- 764 Herzegovina. In *2021 7th International Conference on Control, Instrumentation and*
- 765 *Automation (ICCIA)* (pp. 1–6). <https://doi.org/10.1109/ICCIA52082.2021.9403565>
- 766 Huscroft, J., Gleeson, T., Hartmann, J., & Börker, J. (2018). Compiling and mapping global
- 767 permeability of the unconsolidated and consolidated Earth: GLobal HYdrogeology MaPS
- 768 2.0 (GLHYMPS 2.0). *Geophysical Research Letters*, 45(4), 1897–1904.
- 769 <https://doi.org/10.1002/2017GL075860>
- 770 International Panel on Climate Change (IPCC). (2012). *Managing the Risks of Extreme Events*
- 771 *and Disasters to Advance Climate Change Adaptation* (p. 582). Retrieved from

772           <https://www.ipcc.ch/report/managing-the-risks-of-extreme-events-and-disasters-to->  
773           advance-climate-change-adaptation/

774       Ji, X., Lesack, L., Melack, J. M., Wang, S., Riley, W. J., & Shen, C. (2019). Seasonal and inter-  
775           annual patterns and controls of hydrological fluxes in an Amazon floodplain lake with a  
776           surface-subsurface processes model. *Water Resources Research*, 55(4), 3056–3075.  
777           <https://doi.org/10/gghp4s>

778       Jia, X., Zwart, J., Sadler, J., Appling, A., Oliver, S., Markstrom, S., et al. (2021). Physics-Guided  
779           Recurrent Graph Model for Predicting Flow and Temperature in River Networks. In  
780           *Proceedings of the 2021 SIAM International Conference on Data Mining (SDM)* (pp.  
781           612–620). Society for Industrial and Applied Mathematics.  
782           <https://doi.org/10.1137/1.9781611976700.69>

783       Johnson, J. M., Munasinghe, D., Eyelade, D., & Cohen, S. (2019). An integrated evaluation of  
784           the National Water Model (NWM)–Height Above Nearest Drainage (HAND) flood  
785           mapping methodology. *Natural Hazards and Earth System Sciences*, 19(11), 2405–  
786           2420. <https://doi.org/10.5194/nhess-19-2405-2019>

787       Kalyanapu, A. J., Burian, S. J., & McPherson, T. N. (2009). Effect of land use-based surface  
788           roughness on hydrologic model output. *Journal of Spatial Hydrology*, 9(2), 51–71.  
789           Retrieved from <https://scholarsarchive.byu.edu/josh/vol9/iss2/2>

790       Khorashadi Zadeh, F., Nossent, J., Sarrazin, F., Pianosi, F., van Griensven, A., Wagener, T., &  
791           Bauwens, W. (2017). Comparison of variance-based and moment-independent global  
792           sensitivity analysis approaches by application to the SWAT model. *Environmental  
793           Modelling & Software*, 91, 210–222. <https://doi.org/10.1016/j.envsoft.2017.02.001>

794       Kingma, D. P., & Ba, J. (2017, January 29). Adam: A method for stochastic optimization. arXiv.  
795           <https://doi.org/10.48550/arXiv.1412.6980>

- 796 Koks, E. E., & Thissen, M. (2016). A multiregional impact assessment model for disaster  
797 analysis. *Economic Systems Research*, 28(4), 429–449.  
798 <https://doi.org/10.1080/09535314.2016.1232701>
- 799 Kratzert, F., Klotz, D., Shalev, G., Klambauer, G., Hochreiter, S., & Nearing, G. (2019). Towards  
800 learning universal, regional, and local hydrological behaviors via machine learning  
801 applied to large-sample datasets. *Hydrology and Earth System Sciences*, 23(12), 5089–  
802 5110. <https://doi.org/10.5194/hess-23-5089-2019>
- 803 Leopold, L. B., & Maddock, T. Jr. (1953). The hydraulic geometry of stream channels and some  
804 physiographic implications. *USGS Professional Paper*, 252. <https://doi.org/10/ggj7hw>
- 805 Leshno, M., Lin, V. Ya., Pinkus, A., & Schocken, S. (1993). Multilayer feedforward networks with  
806 a nonpolynomial activation function can approximate any function. *Neural Networks*,  
807 6(6), 861–867. <https://doi.org/10/bjjdg2>
- 808 Li, H., Wigmosta, M. S., Wu, H., Huang, M., Ke, Y., Coleman, A. M., & Leung, L. R. (2013). A  
809 physically based runoff routing model for land surface and earth system models. *Journal*  
810 *of Hydrometeorology*, 14(3), 808–828. <https://doi.org/10/ggj7ph>
- 811 Li, H.-Y., Tan, Z., Ma, H., Zhu, Z., Abeshu, G. W., Zhu, S., et al. (2022). A new large-scale  
812 suspended sediment model and its application over the United States. *Hydrology and*  
813 *Earth System Sciences*, 26(3), 665–688. <https://doi.org/10.5194/hess-26-665-2022>
- 814 Lin, G.-Y., Chen, H.-W., Chen, B.-J., & Yang, Y.-C. (2022). Characterization of temporal PM2.5,  
815 nitrate, and sulfate using deep learning techniques. *Atmospheric Pollution Research*,  
816 13(1), 101260. <https://doi.org/10.1016/j.apr.2021.101260>
- 817 Liu, J., Rahmani, F., Lawson, K., & Shen, C. (2022). A multiscale deep learning model for soil  
818 moisture integrating satellite and in situ data. *Geophysical Research Letters*, 49(7),  
819 e2021GL096847. <https://doi.org/10.1029/2021GL096847>
- 820 Liu, L., Ao, T., Zhou, L., Takeuchi, K., Gusyev, M., Zhang, X., et al. (2022). Comprehensive  
821 evaluation of parameter importance and optimization based on the integrated sensitivity

- analysis system: A case study of the BTOP model in the upper Min River Basin, China.
- Journal of Hydrology*, 610, 127819. <https://doi.org/10.1016/j.jhydrol.2022.127819>
- Martinez, G. F., & Gupta, H. V. (2010). Toward improved identification of hydrological models: A diagnostic evaluation of the “abcd” monthly water balance model for the conterminous United States. *Water Resources Research*, 46(8).  
<https://doi.org/10.1029/2009WR008294>
- Mays, L. W. (2010). *Water Resources Engineering* (2nd edition). Tempe, AZ: Wiley.
- Mays, L. W. (2019). *Water Resources Engineering* (3rd edition). Tempe, AZ: Wiley. Retrieved from <https://www.wiley.com/en-us/Water+Resources+Engineering%2C+3rd+Edition-p-9781119493167>
- Meyal, A. Y., Versteeg, R., Alper, E., Johnson, D., Rodzianko, A., Franklin, M., & Wainwright, H. (2020). Automated cloud based long short-term memory neural network based SWE prediction. *Frontiers in Water*, 2. <https://doi.org/10.3389/frwa.2020.574917>
- Mizukami, N., Clark, M. P., Sampson, K., Nijssen, B., Mao, Y., McMillan, H., et al. (2016). mizuRoute version 1: A river network routing tool for a continental domain water resources applications. *Geoscientific Model Development*, 9(6), 2223–2238.  
<https://doi.org/10.5194/gmd-9-2223-2016>
- Moore, R. B., & Dewald, T. G. (2016). The road to NHDPlus — Advancements in digital stream networks and associated catchments. *JAWRA Journal of the American Water Resources Association*, 52(4), 890–900. <https://doi.org/10.1111/1752-1688.12389>
- Nash, J. E., & Sutcliffe, J. V. (1970). River flow forecasting through conceptual models part I — A discussion of principles. *Journal of Hydrology*, 10(3), 282–290.  
<https://doi.org/10/fbg9tm>
- O, S., & Orth, R. (2021). Global soil moisture data derived through machine learning trained with in-situ measurements. *Scientific Data*, 8(1), 170. <https://doi.org/10.1038/s41597-021-00964-1>

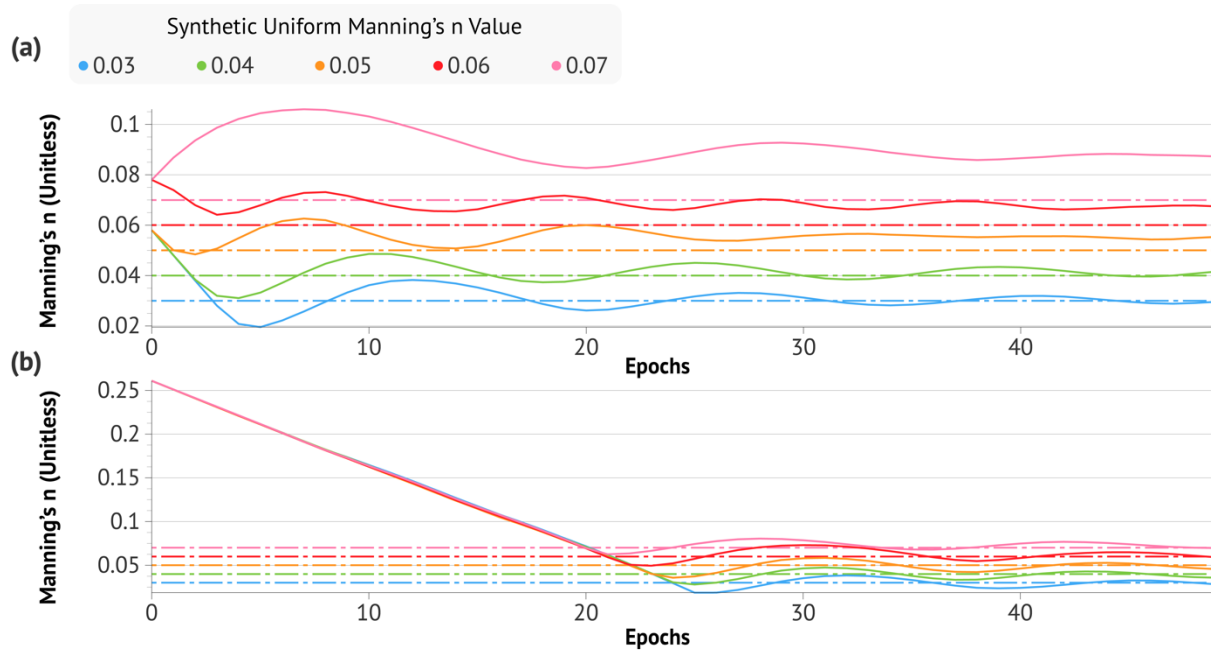
- 848 Ouyang, W., Lawson, K., Feng, D., Ye, L., Zhang, C., & Shen, C. (2021). Continental-scale  
849 streamflow modeling of basins with reservoirs: Towards a coherent deep-learning-based  
850 strategy. *Journal of Hydrology*, 599, 126455.  
851 <https://doi.org/10.1016/j.jhydrol.2021.126455>
- 852 Pan, M., & Wood, E. F. (2013). Inverse streamflow routing. *Hydrology and Earth System  
853 Sciences*, 17(11), 4577–4588. <https://doi.org/10/f5k6nq>
- 854 Prein, A. F., Rasmussen, R. M., Ikeda, K., Liu, C., Clark, M. P., & Holland, G. J. (2017). The  
855 future intensification of hourly precipitation extremes. *Nature Climate Change*, 7(1), 48–  
856 52. <https://doi.org/10.1038/nclimate3168>
- 857 Rahmani, F., Shen, C., Oliver, S., Lawson, K., & Appling, A. (2021). Deep learning approaches  
858 for improving prediction of daily stream temperature in data-scarce, unmonitored, and  
859 dammed basins. *Hydrological Processes*, 35(11), e14400.  
860 <https://doi.org/10.1002/hyp.14400>
- 861 Rahmani, F., Lawson, K., Ouyang, W., Appling, A., Oliver, S., & Shen, C. (2021). Exploring the  
862 exceptional performance of a deep learning stream temperature model and the value of  
863 streamflow data. *Environmental Research Letters*. <https://doi.org/10.1088/1748-9326/abd501>
- 865 Regan, R. S., Markstrom, S. L., Hay, L. E., Viger, R. J., Norton, P. A., Driscoll, J. M., &  
866 LaFontaine, J. H. (2018). *Description of the National Hydrologic Model for use with the  
867 Precipitation-Runoff Modeling System (PRMS)* (No. 6-B9). *Techniques and Methods*.  
868 U.S. Geological Survey. <https://doi.org/10.3133/tm6B9>
- 869 Rice, D. (2019, May 28). Mississippi River flood is longest-lasting in over 90 years, since “Great  
870 Flood” of 1927. *USA Today*. Retrieved from  
871 <https://www.usatoday.com/story/news/nation/2019/05/28/mississippi-river-flooding-longest-lasting-since-great-flood-1927/1261049001/>

- 873 Saha, G. K., Rahmani, F., Shen, C., Li, L., & Cibin, R. (2023). A deep learning-based novel  
874 approach to generate continuous daily stream nitrate concentration for nitrate data-  
875 sparse watersheds. *Science of The Total Environment*, 878, 162930.  
876 <https://doi.org/10.1016/j.scitotenv.2023.162930>
- 877 Shen, C., & Lawson, K. (2021). Applications of Deep Learning in Hydrology. In *Deep Learning*  
878 *for the Earth Sciences* (pp. 283–297). John Wiley & Sons, Ltd.  
879 <https://doi.org/10.1002/9781119646181.ch19>
- 880 Shen, C., & Phanikumar, M. S. (2010). A process-based, distributed hydrologic model based on  
881 a large-scale method for surface–subsurface coupling. *Advances in Water Resources*,  
882 33(12), 1524–1541. <https://doi.org/10/c4r8k5>
- 883 Shen, C., Niu, J., & Phanikumar, M. S. (2013). Evaluating controls on coupled hydrologic and  
884 vegetation dynamics in a humid continental climate watershed using a subsurface - land  
885 surface processes model. *Water Resources Research*, 49(5), 2552–2572.  
886 <https://doi.org/10/f5gcrx>
- 887 Shen, C., Niu, J., & Fang, K. (2014). Quantifying the effects of data integration algorithms on the  
888 outcomes of a subsurface–land surface processes model. *Environmental Modelling &*  
889 *Software*, 59, 146–161. <https://doi.org/10/ggj7mp>
- 890 Shen, C., Riley, W. J., Smithgall, K. M., Melack, J. M., & Fang, K. (2016). The fan of influence of  
891 streams and channel feedbacks to simulated land surface water and carbon dynamics.  
892 *Water Resources Research*, 52(2), 880–902. <https://doi.org/10/f8gppj>
- 893 Shen, C., Chen, X., & Laloy, E. (2021). Editorial: Broadening the use of machine learning in  
894 hydrology. *Frontiers in Water*, 3. <https://doi.org/10.3389/frwa.2021.681023>
- 895 Shen, C., Fang, K., Feng, D., & Bindas, T. (2021). mhpi/hydroDL: MHPI-hydroDL [Data set].  
896 Zenodo. <https://doi.org/10.5281/zenodo.5015120>

- 897 Sun, A. Y., Jiang, P., Mudunuru, M. K., & Chen, X. (2021). Explore spatio-temporal learning of  
898 large sample hydrology using graph neural networks. *Water Resources Research*,  
899 57(12), e2021WR030394. <https://doi.org/10.1029/2021WR030394>
- 900 Sun, A. Y., Jiang, P., Yang, Z.-L., Xie, Y., & Chen, X. (2022). A graph neural network approach  
901 to basin-scale river network learning: The role of physics-based connectivity and data  
902 fusion. *Hydrology and Earth System Sciences Discussions*. <https://doi.org/10.5194/hess-2022-111>
- 904 Tsai, W.-P., Feng, D., Pan, M., Beck, H., Lawson, K., Yang, Y., et al. (2021). From calibration to  
905 parameter learning: Harnessing the scaling effects of big data in geoscientific modeling.  
906 *Nature Communications*, 12(1), 5988. <https://doi.org/10.1038/s41467-021-26107-z>
- 907 US Army Corps of Engineers. (2018). National Inventory of Dams (NID) [Data set]. Retrieved  
908 from <https://nid.sec.usace.army.mil/>
- 909 USGS ScienceBase-Catalog. (2022). National Elevation Dataset (NED). Retrieved September  
910 13, 2022, from <https://www.sciencebase.gov/catalog/item/4fcf8fd4e4b0c7fe80e81504>
- 911 Virtanen, P., Gommers, R., Oliphant, T. E., Haberland, M., Reddy, T., Cournapeau, D., et al.  
912 (2020). SciPy 1.0: fundamental algorithms for scientific computing in Python. *Nature Methods*,  
913 17(3), 261–272. <https://doi.org/10.1038/s41592-019-0686-2>
- 914 Winsemius, H. C., Aerts, J. C. J. H., van Beek, L. P. H., Bierkens, M. F. P., Bouwman, A.,  
915 Jongman, B., et al. (2016). Global drivers of future river flood risk. *Nature Climate Change*,  
916 6(4), 381–385. <https://doi.org/10.1038/nclimate2893>
- 917 Wunsch, A., Liesch, T., & Broda, S. (2022). Deep learning shows declining groundwater levels  
918 in Germany until 2100 due to climate change. *Nature Communications*, 13(1), 1221.  
919 <https://doi.org/10.1038/s41467-022-28770-2>
- 920 Xia, Y., Mitchell, K., Ek, M., Sheffield, J., Cosgrove, B., Wood, E., et al. (2009). NLDAS Primary  
921 Forcing Data L4 Hourly 0.125 x 0.125 degree V002 (NLDAS\_FORA0125\_H) [Data set].

- 922 Goddard Earth Sciences Data and Information Services Center (GES DISC).  
923 <https://doi.org/10.5067/6J5LHHOHZHN4>
- 924 Xia, Y., Mitchell, K., Ek, M., Sheffield, J., Cosgrove, B., Wood, E., et al. (2012). Continental-  
925 scale water and energy flux analysis and validation for the North American Land Data  
926 Assimilation System project phase 2 (NLDAS-2): 1. Intercomparison and application of  
927 model products. *Journal of Geophysical Research: Atmospheres*, 117(D3).  
928 <https://doi.org/10.1029/2011JD016048>
- 929 Xiang, Z., Yan, J., & Demir, I. (2020). A rainfall-runoff model with LSTM-based sequence-to-  
930 sequence learning. *Water Resources Research*, 56(1), e2019WR025326.  
931 <https://doi.org/10.1029/2019WR025326>
- 932 Ye, A., Zhou, Z., You, J., Ma, F., & Duan, Q. (2018). Dynamic Manning's roughness coefficients  
933 for hydrological modelling in basins. *Hydrology Research*, 49(5), 1379–1395.  
934 <https://doi.org/10.2166/nh.2018.175>
- 935 Zhi, W., Feng, D., Tsai, W.-P., Sterle, G., Harbold, A., Shen, C., & Li, L. (2021). From  
936 hydrometeorology to river water quality: Can a deep learning model predict dissolved  
937 oxygen at the continental scale? *Environmental Science & Technology*, 55(4), 2357–  
938 2368. <https://doi.org/10.1021/acs.est.0c06783>
- 939 Zhu, F., Li, X., Qin, J., Yang, K., Cuo, L., Tang, W., & Shen, C. (2021). Integration of  
940 multisource data to estimate downward longwave radiation based on deep neural  
941 networks. *IEEE Transactions on Geoscience and Remote Sensing*, 1–15.  
942 <https://doi.org/10.1109/TGRS.2021.3094321>
- 943

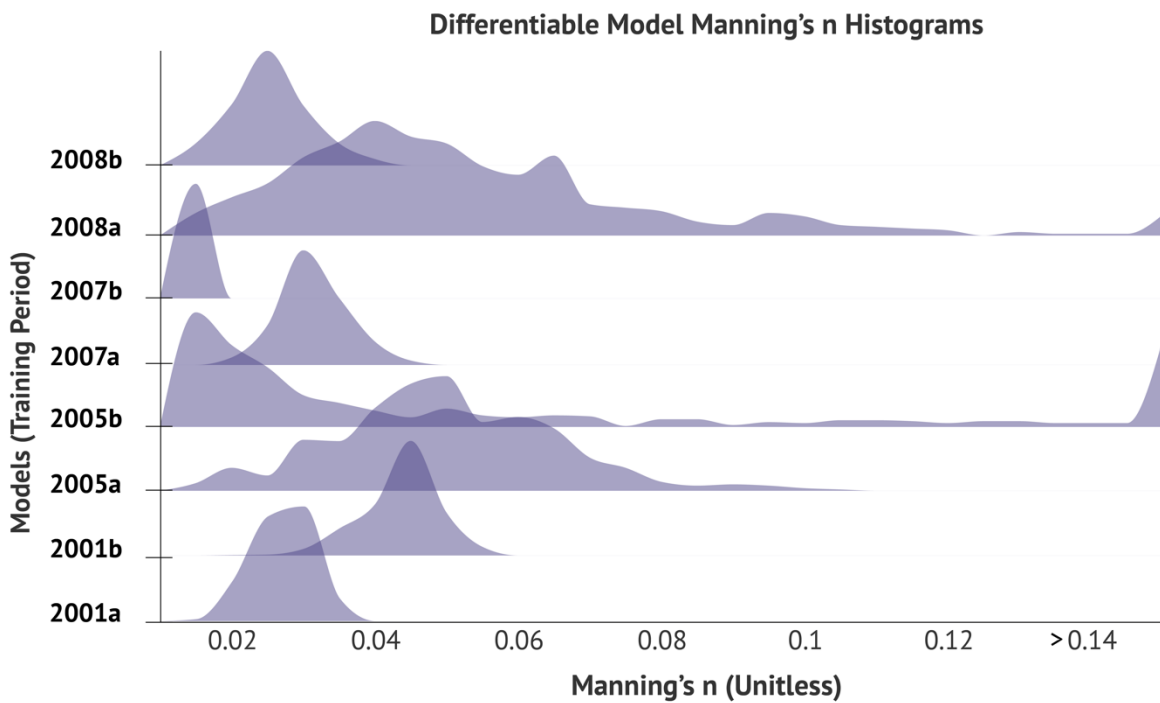
944 **Appendix**



945  
946

947 Figure A1: The synthetic parameter recovery of Manning's  $n$  after each epoch run, with each colored line  
948 representing a different recovered value. (a) The initial value of  $n$  is set to 0.068 (b) the initial value of  $n$   
949 is set to 0.271

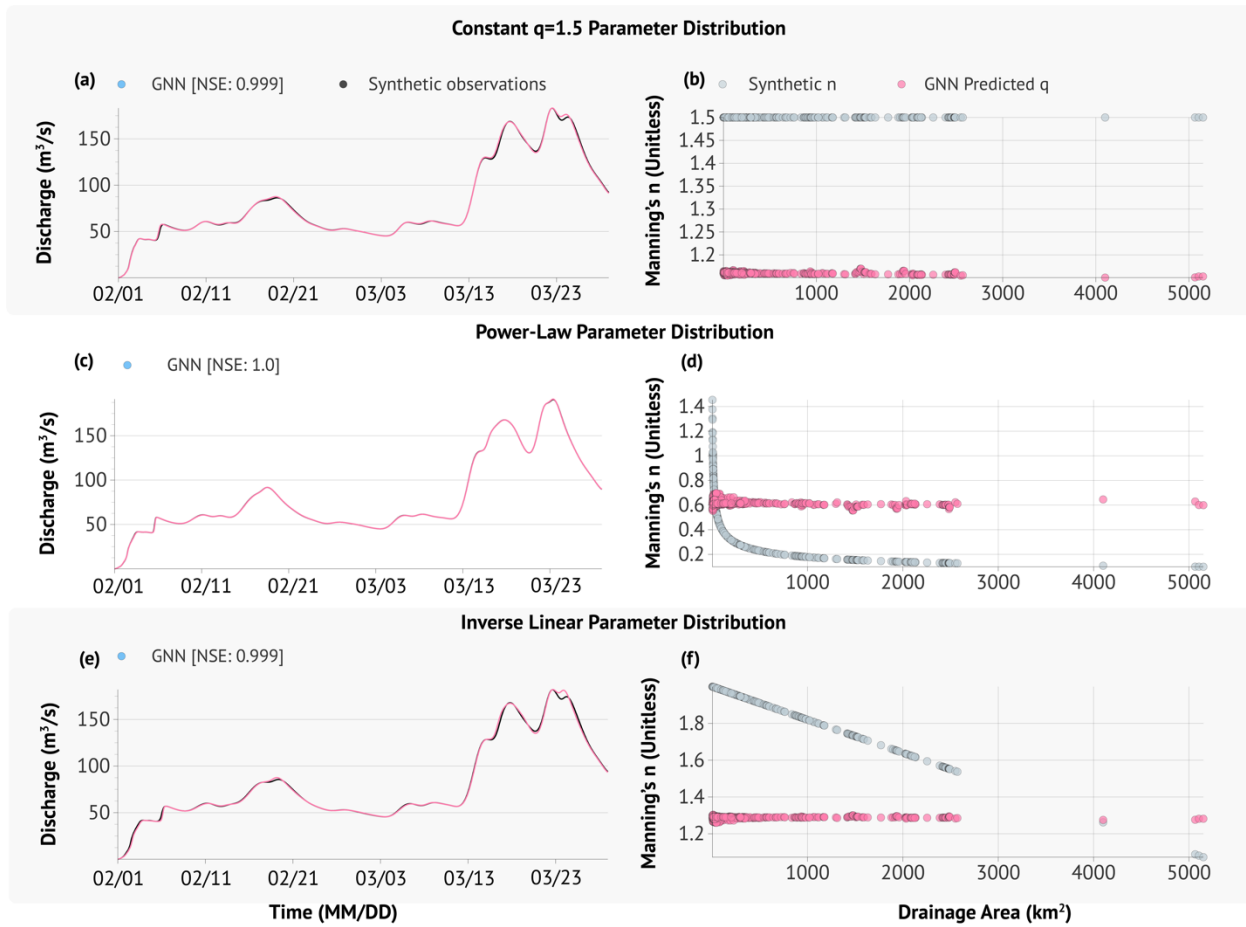
950



951

952 Figure A2: Histograms visualizing the frequency, and variability, of Manning's  $n$  values for all river  
 953 reaches (582 total) for all eight GNN models. The lower bound is 0.01, while the upper bound contains  
 954 all Manning's  $n$  values  $>0.14$ .

955



956  
 957 Figure A3: Results from  $q$  parameter recovery experiments. We tried to recover both constant and  
 958 distributed parameters, but were unable to ever recover the synthetic truth.

959

960 Table A1: The attributes and forcings used by the pre-trained LSTM to predict streamflow. Links to the  
 961 data can be found below the table

Attribute/Meteorological Forcing	Unit	Dataset	Citation
Mean Elevation	m	SRTMGL1	(Carabajal & Harding, 2006)
Mean Slope	unitless	SRTMGL1	(Carabajal & Harding, 2006)

Basin Area	km <sup>2</sup>	SRTMGL1	(Carabajal & Harding, 2006)
Dominant Land Cover	Class	MODIS	(Friedl & Sulla-Menashe, 2019)
Dominant Land Cover Fraction	Percent	MODIS	(Friedl & Sulla-Menashe, 2019)
Forest Fraction	Percent	MODIS	(Friedl & Sulla-Menashe, 2019)
Root Depth (50)	m	MODIS	(Friedl & Sulla-Menashe, 2019)
Soil Depth	m	MODIS	(Friedl & Sulla-Menashe, 2019)
Ksat (0-5)	log <sub>10</sub> (cm/hr)	POLARIS	(Chaney et al., 2019)
Ksat (5-15)	log <sub>10</sub> (cm/hr)	POLARIS	(Chaney et al., 2019)
Theta s (0-5)	m <sup>3</sup> /m <sup>3</sup>	POLARIS	(Chaney et al., 2019)
Theta s (5-15)	m <sup>3</sup> /m <sup>3</sup>	POLARIS	(Chaney et al., 2019)
Theta r (5-15)	m <sup>3</sup> /m <sup>3</sup>	POLARIS	(Chaney et al., 2019)
Ksat average (0-15)	log <sub>10</sub> (cm/hr)	POLARIS	(Chaney et al., 2019)
Ksat e (0-5)	cm/hr	POLARIS	(Chaney et al., 2019)

Ksat e (5-15)	cm/hr	POLARIS	(Chaney et al., 2019)
Ksat average e (0-15)	cm/hr	POLARIS	(Chaney et al., 2019)
Theta average s (0-15)	$\epsilon^{m^3/m^3}$	POLARIS	(Chaney et al., 2019)
Theta average r (0-15)	$\epsilon^{m^3/m^3}$	POLARIS	(Chaney et al., 2019)
Porosity	Percent	GLHYMPS	(Huscroft et al., 2018)
Permeability Permafrost	$m^2$	GLHYMPS	(Huscroft et al., 2018)
Permeability Permafrost (Raw)	$m^2$	GLHYMPS	(Huscroft et al., 2018)
Major Number of Dams	Unitless	GAGES-II	(Falcone, 2011)
General Purpose of Dam	Unitless	National Inventory of Dams (NID)	(US Army Corps of Engineers, 2018)
Max of Normal Storage	Acre-ft	National Inventory of Dams (NID)	(US Army Corps of Engineers, 2018)
Standard Deviation of Normal Storage	Unitless	National Inventory of Dams (NID)	(US Army Corps of Engineers, 2018)
Number of dams within river (2009)	Unitless	GAGES-II	(Falcone, 2011)
Normal Storage (2009)	Acre-ft	National Inventory of Dams (NID)	(US Army Corps of Engineers, 2018)
Precipitation hourly total	$kg/m^2$	NLDAS2	(Xia et al., 2012)
Surface downward longwave radiation	$W/m^2$	NLDAS2	(Xia et al., 2012)

Surface downward shortwave radiation	W/m <sup>2</sup>	NLDAS2	(Xia et al., 2012)
Pressure	Pa	NLDAS2	(Xia et al., 2012)
Air Temperature	K	NLDAS2	(Xia et al., 2012)

962

963 SRTMGL1: <https://doi.org/10.14358/PERS.72.3.287>964 MODIS: <https://modis.gsfc.nasa.gov/data/dataproducts/mod12.php>965 POLARIS: <https://doi.org/10.1029/2018WR022797>966 GLHYMPS: <https://doi.org/10.5683/SP2/DLGXYO>967 NID: <https://nid.usace.army.mil/>968 NLDAS2: <https://ldas.gsfc.nasa.gov/nldas/v2/forcing>

969

970 970 Table A2: The constant attributes ( $c$ ) used by the MLP to predict  $n$  and  $q$ :  $n, q = NN(c)$ .

Attribute	Unit
Reach Width	m
Average-Reach Elevation	m
Slope	m/m
Reach Area	km <sup>2</sup>
Total Drainage Area	km <sup>2</sup>
Reach Length	m
Sinuosity	m/m
Bank Elevation	m

971

972 Table A3: The  $\Sigma Q^*$  ( $\tau = 9$ ) NSE scores for all eight training time periods for the most downstream gage.973 Since  $Q^*$  routing is a pure forward simulation using the trained LSTM, we report the NSE values for each  
974 period.

975

	Periods							
	2001a	2001b	2005a	2005b	2007a	2007b	2008a	2008b
NSE	0.5958	0.3534	-0.7868	-0.1687	0.6830	0.0558	-0.4297	0.3792

